Optical Properties of Hybrid Nanomaterials

by

Adam H. Blake

A Dissertation Presented in Partial Fulfillment
of the Requirements for the Degree
Doctor of Philosophy

Approved November 2016 by the
Graduate Supervisory Committee:

Maxim Sukharev, Chair
Mike Treacy
Igor Shovkovy
Jeff Drucker

ARIZONA STATE UNIVERSITY

December 2016

ABSTRACT

The interaction of light with nanoscale structures consisting of metal and two-level quantum emitters is investigated computationally. A method of tilting the incoming electromagnetic wave is used to demonstrate coupling between a sinusoidal grating and two-level quantum emitters. A system consisting of metallic v-grooves and two-level emitters is thoroughly explored in the linear regime, where the spatially uniform fields provide a unique means of characterizing the coupling between the v-grooves and emitters. Furthermore, subwavelength spatial effects in the ground state population of emitters in the v-grooves are observed and analyzed in the non-linear regime. Finally, photon echoes are explored in the case of a one-dimensional ensemble of interacting two-level emitters as well as two-level emitters coupled to metallic slits, demonstrating the influence of collective effects on the echo amplitude in the former and the modification of the photon echo due to interaction with surface plasmons on the slits in the latter.

To Dad, Mom, Sam, Yuliya, Alyssa, and Riley.

TABLE OF CONTENTS

LIST OF FIGURES

vi

Figure Page

Chapter 1

INTRODUCTION

1.1 Motivation

This chapter presents a review of theory and literature that is relevant to the study of hybrid nanoscale systems. This work was published in Blake and Sukharev (2015a) and Blake and Sukharev (2015b).

Plasmonics offers the potential for the creation and control of signals at the very smallest of scales. Plasmonic versions of waveguides (Fernandez-Cuesta *et al.*, 2009), switches (Vasa *et al.*, 2010), and lasers (Pusch *et al.*, 2012) are being considered theoretically and experimentally. When excited optically, the wavelength of the corresponding plasmonic effects can be smaller than that of the optical fields. We therefore view plasmonics as a promising means around the diffraction limit.

The work presented herein is potentially useful in several respects. Simulations are usually much easier to perform than experiments, and can thus guide time- and labor-intensive experiments and reduce trial-and-error. Tilting the incident wave is a ubiquitous means of examining the coupling that is present in hybrid systems, and this can now be accomplished in our simulations. Slow light has been shown in our simulations to influence the optical properties of hybrid systems, and one can imagine precisely and uniquely configuring very small regions via application of different laser pulses. Photon echoes are used to study, among other things, the time dynamics of chemical reactions. We are able to reproduce this phenomenon in our simulations and manipulate it as desired. The final chapter extends this to 1-D ensembles of interacting two-level emitters as well as hybrid systems; these are

previously unexplored frontiers of the non-linear regime.

1.2   Surface Plasmon Polaritons

Surface plasmon polaritons (SPPs) are oscillations of charge on a metal-dielectric boundary that are able to produce intense, highly localized evanescent fields. SPPs can be described classically, but the name derives from the more accurate quantum mechanical description. A quantum of surface charge oscillation (a plasmon) couples to a quantum of light (a photon) leading to a system that is a hybrid of the two independent entities: a surface plasmon polariton.

Maxwell's equations are applied to the interface between a dielectric and a metal in Raether (1988), leading to a dispersion relation for SPPs:

$$k_x = \frac{\omega}{c} \sqrt{\frac{\epsilon_1 \epsilon_2}{\epsilon_1 + \epsilon_2}} \tag{1.1}$$

ϵ_2 is the permittivity of the dielectric, ϵ_1 is the permittivity of the metal, k_x is the in-plane wave vector of the SPP (the x-direction lies in the plane of the interface; see Fig. 1a), ω is the angular frequency of the SPP, and c is the speed of light in vacuum. The limiting value of ω given $\epsilon_2 = 1.0$ is $\omega_p/\sqrt{2}$, where ω_p is the plasma frequency (the natural frequency of free electron plasma oscillations). The response of the metal, obtained from the Drude model (to be discussed in Chapter 2) is substituted into the above dispersion relation and the curve shown in Fig. 1b is obtained.

SPPs offer a means around the diffraction limit *because as can be seen from the dispersion curve, the wavelength corresponding to the SPP can be made much smaller than that of light for a given frequency of excitation.* (Barnes *et al.*, 2003)

One means of exciting and observing SPPs is via the attenuated total reflection (ATR) method which is discussed extensively in Raether (1988). In order to excite SPPs, the in-plane wave vector of the light must match that of the SPP. This can be

2
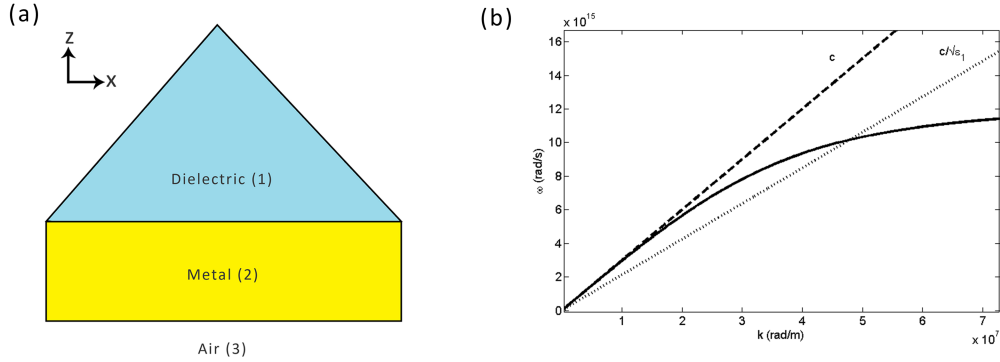
Figure 1.1: Illustration of propagating surface plasmon-polaritons and associated setup. a) A dielectric prism (medium 1) on top of a metal film (medium 2) with air underneath (medium 3). b) Dispersion relation for SPPs formed on an air/metal (2/3) interface. The curve follows the light line for air (with slope c) for low values of k but bends downward and asymptotically approaches $\omega_p/\sqrt{2}$ for large values of k. The dispersion line for light in a dielectric (medium 1, slope $c/\sqrt{\epsilon_1}$) is shown for reference. Not shown is the dispersion relation for SPPs on the metal/dielectric (1/2) interface: this curve lies entirely to the right of the dispersion line for light in the dielectric.

achieved by placing a prism in contact with the top of the metal film (Kretschman-Raether configuration) and having air or vacuum in contact with the bottom of the film: see Fig. 1a. The dielectric (medium 1) has $\epsilon_1 > 1$, the metal (medium 2) has ϵ_2 represented by the Drude model, and air (medium 3) has $\epsilon_3 = 1$. According to the dispersion relation for SPPs on the 1/2 interface (not shown in Fig. 1b), light passing from the prism to the metal film cannot have the same in-plane wave vector k_x as an SPP (on the 1/2 interface) of the same frequency because the SPP dispersion curve for the 1/2 interface lies completely to the right of the light line in the dielectric (whose slope is $c/\sqrt{\epsilon_1}$). Light that is incident upon the 1/2 interface can be made to undergo total internal reflection (TIR), and an evanescent wave whose in-plane wave vector equals $\frac{\omega}{c\sin\theta_0\sqrt{\epsilon_1}}$ extends into the metal to the 2/3 boundary. This line corresponding to the dispersion relation of the evanescent wave intersects the SPP

3

dispersion relation for the 2/3 boundary: in other words, the in-plane wave vector of the light is increased to match the in-plane wave vector k_x for an SPP on the 2/3 boundary. SPPs are not excited on the 1/2 interface; the k_x is set at the 1/2 interface and that k_x transfers over to the dispersion relation at the 2/3 interface. One finds that over a certain range of angles beyond the critical angle, reflection is attenuated. This corresponds to the evanescent wave coupling to the SPP on the air-side of the film, which absorbs the radiation and is therefore responsible for the decreased reflection (hence attenuated total reflection).

Besides the ATR method, another means of matching in-plane wave vectors for the purpose of exciting SPPs involves the use of a periodic grating (Garcia de Abajo, 2007). Periodic arrays of slits (Salomon *et al.*, 2012) can be used as well as a periodic sinusoidal grating (Sukharev *et al.*, 2009). The grating modifies the in-plane wave vector of the incident light such that it increases to match that of an SPP mode supported by the grating.

Surface plasmon resonances find numerous applications, especially as biosensors (Jonsson *et al.*, 1991; Haes *et al.*, 2004; Jain *et al.*, 2007; Willets and Van Duyne, 2007; Homola *et al.*, 1999; Rich and Myszka, 2000; Hoa *et al.*, 2007). One common application involves an ATR setup in which biochemically active molecules undergo reaction near the dielectric, changing the index of refraction and causing the ATR minimum to shift. This is a means of observing molecular dynamics.

1.3   Coupled Harmonic Oscillators

The idea of coupled harmonic oscillators is readily demonstrated for macroscopic systems such as two mass-spring systems with a coupling spring between the masses. Two coupled pendulums also serve as a good example. Remarkably, the analytical machinery of coupled harmonic oscillators can be applied in the microscopic domain

to quantum emitters (an atom or molecule that has a well-defined optical transition and can be treated as a two-level atom), charge density waves, and electromagnetic fields. None of these immediately conjures up an image of a mass on a spring. But when emitters and charge density waves are treated as oscillators coupled by the fields that they emit, features predicted by classical coupled oscillator equations, such as strong coupling and avoided crossing, are clearly observed! We therefore have a firm analytical framework for understanding hybrid materials consisting of emitters and metallic structures.

Coupling two oscillators and solving for the eigenfrequencies ω_+ and ω_- yields (Torma and Barnes, 2015):

$$\omega_+^2 \;=\; \omega_c^2 + \Omega^2 \tag{1.2a}$$

$$\omega_-^2 \;=\; \omega_c^2 - \Omega^2 \tag{1.2b}$$

$$\omega_c^2 \;=\; \omega^2 + \Omega^2 \tag{1.2c}$$

ω_c is the frequency that one oscillator would have if the other were held in place, ω is the resonant frequency of each uncoupled oscillator, and Ω describes the coupling strength between the oscillators. Clearly, the splitting between normal mode frequencies increases as the coupling strength is increased.

In the case of coupling emitters to charge density waves such as SPPs, we are dealing with an oscillator and a standing wave. Consider the (separate) dispersion relations of two uncoupled systems: a two-level emitter and an SPP. The dispersion relations for each uncoupled system as well as the coupled system are shown in Fig. 1.2. Each of the solid lines represents the dispersion relation that would be obtained from each individual, independent oscillator. A complete picture of the coupling is given in Torma and Barnes (2015). The Hamiltonian of the coupled exciton-SPP
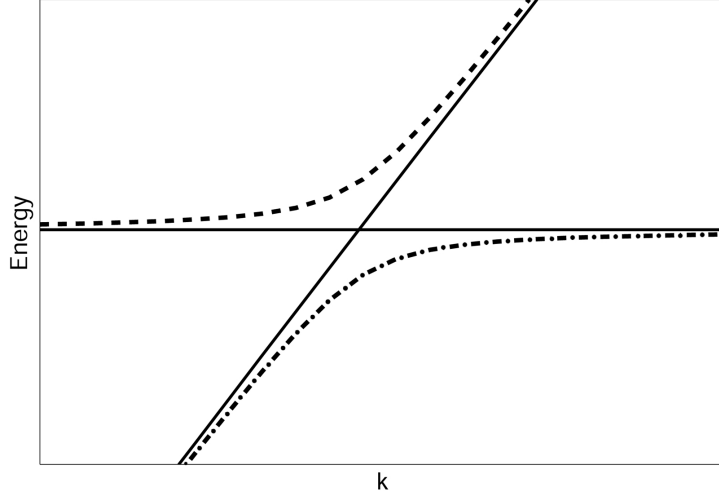
Figure 1.2:   The dispersion relation of an uncoupled SPP (diagonal solid line), two-level emitter (horizontal solid line), and coupled system consisting of the upper polariton (curved dashed line) and lower polariton (curved dash-dot line). Note that at larger wave numbers (not shown here), the SPP dispersion curve bends and asymptotically approaches a constant value.

system is as follows:

$$
\begin{bmatrix}
E_m & \Delta \\
\Delta & E_p(k)
\end{bmatrix}
\tag{1.3}
$$

$E_{pl}(k)$ is the energy of the uncoupled plasmon energy, E_m is the energy of the uncoupled emitter resonance, and Δ is the coupling energy. This Hamiltonian is diagonalized, yielding the following expression for the energies of the normal modes of the system (referred to as upper and lower polaritons) as a function of wave vector (Agranovich *et al.*, 2003; Lidzey *et al.*, 1998):

$$
E_{u,l}(k) = \frac{1}{2}\{[E_{pl}(k) + E_m] \pm \sqrt{4\Delta^2 + (E_{pl}(k) + E_m)^2}\}
\tag{1.4}
$$

$E_{u,l}(k)$ is the energy of the upper or lower polariton as a function of the wave number k and all other quantities are the same as in Eq. 1.3. The minimum energy

separation is the Rabi splitting of the system and this value increases as the coupling strength is increased. Where the solid lines in Fig. 1.2 overlap (i.e. both systems driven at resonance) the dispersion of coupled oscillators clearly departs from that of the uncoupled oscillators. Far from resonance, the system response approaches that of uncoupled oscillators.

This leads to the definition of two regimes: weak coupling and strong coupling. When the coupling strength exceeds the upper and lower polaritons' linewidths, the system is in the strong coupling regime (Torma and Barnes, 2015). If the damping is strong enough that the splitting is not observable, the system is in the weak coupling regime.

We will look at several examples of weak and strong coupling between light and matter, the first of which is emitters in a reflecting microcavity followed by emitters coupled to surface plasmon polaritons via various geometric structures.

1.4   Coupling Microcavities to Quantum Emitters

The emission characteristics of an emitter depend upon the environment in which it is placed. Modifying the environment in which an emitter is placed can be accomplished in many different ways. Photons can be confined inside of one of various configurations of reflecting microcavities. As will be discussed in the next section, an emitter can be placed in the intense fields of an SPP. Some experiments involve shooting atoms through a cavity one at a time, with each atom interacting with the fields from the atom that preceded it (Haroche, 2013). In this section, the coupling of emitters to microcavities is discussed.

Confining emitters to a microcavity was first demonstrated by Efros and Efros (1982) and Ekimov and Onushchenko (1981) in which semiconductor nanocrystals were grown in glass. More elaborate structures have since been developed. Micropil-

7

lars use Bragg mirrors to confine light axially and total internal reflection for radial confinement. Microdisks use total internal reflection for confinement along all directions. Photonic crystals are periodic nanostructures with regions of high and low dielectric constant that can create bandgaps (frequency regions over which propagation is forbidden) for photons. These actually occur naturally as opals. One of the primary differences between these three structures is the size of the emitter (in this case, a quantum dot) that can be placed in the cavity. A larger quantum dot gives a larger dipole moment and therefore stronger coupling. The micropillar and microdisk structures have larger volumes which would lead to weaker coupling were it not for the fact that a larger quantum dot (with a larger dipole moment) can be placed in this larger volume, whereas the photonic crystal offers a smaller volume and higher quality factor Q leading to the largest E-field in the empty cavity (Khitrova *et al.*, 2006).

The spontaneous emission rate of a quantum emitter can be controlled by placing it in a reflecting microcavity (Haroche, 2013). Spontaneous emission is suppressed when the size of the cavity is less than the emission wavelength and enhanced when the size of the cavity is equal to the emission wavelength. The reason for this is that spontaneous emission is actually stimulated by vacuum fluctuations and the size of the cavity determines the wavelengths of vacuum fluctuations that are permitted.

The enhancement of spontaneous emission is known as the Purcell effect and is quantified by the Purcell factor:

$$F_p = \frac{3}{4\pi^2} \frac{\lambda_c^3}{n} \left(Q/V\right) \tag{1.5}$$

λ_c is the wavelength in the cavity medium, n is the index of refraction of the cavity medium, and V is the mode volume of the cavity.

Quantum information science, which requires photon-on-demand sources, can ben-

efit from more deterministic control of photon emission. It is desirable to know exactly when the photon is going to be emitted, and shorter emission lifetimes accomplish this. The Purcell effect increases the emission rate and therefore decreases the emission time, thereby making the emission of the photon more deterministic. As can be seen from Eq. 1.5, this can be realized by increasing the quality factor and decreasing the effective volume of the cavity. The decreasing volume ultimately restricts the cavity to a single mode (Khitrova *et al.*, 2006). Also, the quantum dephasing rate must be made much smaller than the cavity decay rate. If a quantum emitter / microcavity system is to be used for quantum computing, it will ideally demonstrate antibunching (no more than one photon emitted at a time) and uniform spacing between the emitted photons.

When an emitter is strongly coupled to a microcavity, the states of both systems are altered: one system is coupled to another and the original energy levels of each individual system are modified and become that of a single, hybrid system. The extent to which the original energy levels are modified is determined by the coupling between the two systems. Strong coupling between inorganic quantum emitters and microcavities has yielded Rabi splitting of 3-10 meV, whereas strong coupling between organic quantum emitters (such as J-aggregates) and microcavities shows Rabi splitting of 100-500 meV (Agranovich and La Rocca, 2005). Bellessa *et al.* (2004) coupled J-aggregates to a cavity and observed a Rabi splitting of about 300 meV.

The strong coupling regime can be mapped by varying the temperature of the emitter, which sweeps the emitter resonance across that of the microcavity. This is less than ideal, as changing the temperature of the emitter causes its optical properties to change. A less intrusive means of sweeping the emitter resonance involves incrementally condensing Xe onto the interior of the microcavity (Mosor *et al.*, 2005), causing the index of refraction to increase relative to vacuum and the emitter reso-

nance to shift to lower energies.

The dispersion relation for the upper and lower polaritons for a system consisting of an organic semiconductor material inside of a microcavity is derived in Agranovich and La Rocca (2005) and it is equivalent to Eq. 1.4 up to a damping term. This is not surprising; even though one equation deals with SPPs and the other with microcavities, both describe systems of two-level emitters coupled to electromagnetic field modes. The upper and lower polaritons (coherent excitations) are well defined within certain limits of the wave vector k, outside of which (less than k_{min} or larger than k_{max}) wave vector broadening is on the order of the wave vector itself and the excitations become incoherent (Agranovich and La Rocca, 2005). The states of a microcavity whose volume contains an organic semiconductor consist of a mixture of a large number of incoherent states and a smaller number of coherent states. Photoluminescence from the former pumps the latter.

It is emphasized in Agranovich and La Rocca (2005) that the excitations, even when not clearly defined, are coupled exciton-cavity excitations. k_{min} can be reduced for inorganic structures because of the lower damping at lower temperatures. At large wave vectors the upper polariton tends toward the cavity curve. These states are coherent, and the upper polariton can decay into an incoherent state, which can decay into the lower polariton. Either of these processes results in an optical phonon.

1.5   Strong Coupling Between Surface Plasmon Polaritons and Quantum Emitters

After demonstrating the coupling of emitters to microcavities, subsequent experiments were performed in which emitters were coupled to SPPs. Pockrand *et al.* (1982) demonstrated a splitting of the ATR minimum due to coupling between dye molecules and SPPs on a metal film and Bellessa *et al.* (2004) were able to achieve Rabi splitting of the order of that achieved in cavities. Because SPPs have very lo-

10

calized fields corresponding to small effective volumes, strong coupling corresponding to the values observed in small microcavities is achieved without the technical hassle of using small microcavities. The largest Rabi splitting between SPPs and emitters observed thus far is 700 meV (Schwartz *et al.*, 2011). Coupling emitters to SPPs is not a perfect scheme, however. SPP modes are dissipative, allowing only a limited number of Rabi oscillations to take place (Torma and Barnes, 2015).

The coupling strength can be influenced by the dipole moment of the emitters, the density of emitters, and the effective volume (originally associated with the volume of a reflecting cavity in which emitters were placed) of the fields. A specific description of the coupling strength between SPP modes and emitters is given in Vasa *et al.* (2013):

$$\hbar\Omega_R = \sqrt{N_x}\vec{\mu_x} \cdot \vec{E_v} \tag{1.6}$$

where $\vec{E_v}$ is the SPP vacuum field, Ω_R is the Rabi splitting, μ_x is the transition dipole moment and N_x is the number of excitons. A calculation in Torma and Barnes (2015), which analyzes the SPP dispersion relation and solves for the normal mode frequencies, shows that the splitting of normal mode frequencies is proportional to $\sqrt{N_x}$. The strong coupling regime is defined in Torma and Barnes (2015) as when the normal mode splitting ($\Omega_{NMS} \approx \Omega_R$) exceeds all of the damping rates (and therefore linewidths) in the system.

A departure from the usual normal mode splitting occurs when either or both emitter density and emitter dipole moment (increasing either of these increases coupling between SPPs and emitters) are made very large (Salomon *et al.*, 2012). Ordinary normal mode splitting is demonstrated by using lower values of emitter density and dipole moment and varying the period of the slit array (which is experimentally adjustable), causing the SPP resonance to shift. The SPP resonance is swept

through the emitter resonance, demonstrating avoided crossing. This however assumes interaction between SPPs and isolated emitters. The interaction between the emitters themselves increases as emitter density and dipole moment increase and in fact, the accuracy of the two-level model begins to suffer as the emitter density and / or dipole moment increases. For the case of ordinary normal mode splitting (no interaction between the emitters), the Rabi splitting increases linearly as $\sqrt{N}$ (Torma and Barnes, 2015; Vasa *et al.*, 2013), where N is the emitter density. Simulations from Salomon *et al.* (2012) show deviations from this behavior at high emitter densities. Rabi splitting increases linearly with the dipole moment, and deviations are not seen in Salomon *et al.* (2012) at higher dipole moments.

In addition to the deviations mentioned, a new peak appears in between the upper and lower polaritons and it is proposed to indicate a collective effect from the entire ensemble of emitters. The progression from ordinary Rabi splitting to the appearance of the collective peak is shown in Fig. 1.3. Experiments verify that this third peak is present under conditions of very strong coupling (Salomon *et al.*, 2009; Sugawara *et al.*, 2006; Hutchison *et al.*, 2011). It does not deviate appreciably from the emitter resonance even as the SPP resonance is tuned, suggesting that its origin is from the emitters rather than the SPPs. An energy gap is also observed: when the coupling strength is such that the collective mode is not seen, the upper and lower polariton energies asymptotically approach the emitter resonance for large detuning. When the collective peak is present, the asymptotes of the upper and lower polaritons (for large detuning) have a gap between them. The upper polariton demonstrates a larger gap than the lower polariton.

A spacer layer of variable thickness was inserted between the emitter layer and the grating in order to see the dependence of emitter-emitter coupling on the strength of the SPP field. The collective peak is observed to merge with the upper polariton as
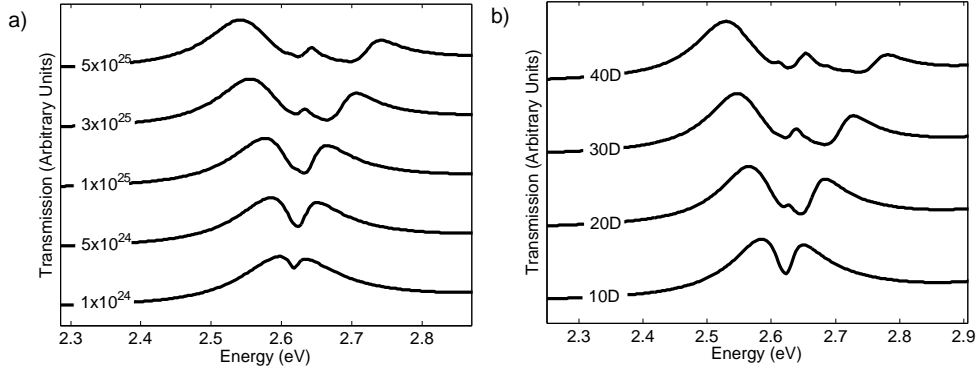
Figure 1.3: Emitter density and dipole moment affect the coupling between SPPs and emitters. The raw data is taken from Salomon *et al.* (2012). Panel (a) shows increasing emitter density (emitters per m^3) and panel (b) shows increasing emitter dipole moment. When either the density or dipole moment are low, "ordinary" Rabi splitting is seen. As density or dipole moment is increased, the third "collective" peak emerges and strengthens near the emitter resonance.

the spacer thickness increases. Coupling between the emitters themselves is suspected given the fall-off of the collective mode as the SPP field decreases. Furthermore, a simulation was run in which the entire region containing emitters was replaced by a single two-level system (essentially a single quantum emitter with a very large dipole moment), thereby eliminating the spatial variation of the fields. In this case, the collective peak disappears even at extremely high emitter densities.

1.6   Control and Time Dynamics of Strong Coupling

The emission from quantum dots is essentially isotropic, but results shown in Livneh *et al.* (2011) demonstrate that depositing quantum dots onto a periodic slit array causes the dots' emission to become both directional and wavelength-selective. Quantum dots have also been placed upon a nanoscale Yagi-Uda antenna (Curto *et al.*, 2010).

An aluminum grating on a glass substrate is used, and the emitters are InAs /

CdSe core-shell nanocrystal quantum dots (NQDs). The emission spectrum of the NQDs peaks at 1.2 μm and has a FWHM of about 200 nm with no angular dependence being observed.

A plot of near-field intensity (as seen in Fig. 3 in Livneh *et al.* (2011)) for the NQD/slit system shows intense fields near the slits at zero angle from the slits and much weaker fields at 15 degrees. A plot of emission intensity vs. incident angle (as seen in Fig. 3 in Livneh *et al.* (2011)) shows a FWHM of 3.4 degrees and transmission in the forward direction that is 20 times higher than a sample consisting only of NQDs. This beaming effect is thought to be a result of the NQDs being coupled to the SPP waves.

As stated previously, coupling can be manipulated by changing $\vec{\mu}_x$ or $\vec{E}_{SPP}$ and Vasa *et al.* (2010) takes advantage of this in order to create an optically switchable metallic mirror. By altering the dipole moment of the emitters (and thus the coupling) on short timescales, the reflection can be reduced by 40% in parts of the near-infrared. This is a reversible, sub-picosecond effect which is immediately appealing as a switch, especially given that it can be controlled by a single photon.

Results are first presented for J-aggregates on a smooth gold film. At the emitter resonance, the bare film displays a reflectivity of 0.95, which drops to 0.25 when the emitters are added. With a pump pulse, the reflectance (relative to that of the bare film) at the emitter resonance is seen to increase for all values of pump fluence. A system of J-aggregates deposited upon a gold reflection grating is subsequently analyzed. A contour plot of reflectivity as a function of angle of incidence and wavelength (as seen in Fig. 2 in Vasa *et al.* (2010)) shows an avoided crossing which of course indicates strong coupling between the emitters and the SPPs, and calculations show that the SPP fields are localized around the slits. The spectra obtained agree with numerical solutions of Maxwell's equations as applied to the hybrid structure. Non-

equilibrium time dynamics is then detailed: a pump pulse is sent in first, followed by a probe pulse 150 fs later. Near the exciton resonance, the reflection behaves as that of the emitters on a smooth film; these excitons are therefore not strongly coupled to the SPP fields. The usual upper and lower polariton features remain, but additional structure (minima in reflections) is seen in these curves. As the pump fluence is increased, these new features separate from the upper and lower polariton curves and begin to resemble those of uncoupled oscillators. This can be understood in terms of a decrease in coupling strength of the excitons that are strongly coupled to the SPP field, as a reduction in the dipole moment occurs due to saturation of the excitonic oscillator strength. Note that the pumping is non-resonant; it is on the tail of the exciton curve. This creates a mixture of uncoupled and coupled excitons.

A pump pulse can therefore switch the system from well-defined upper and lower polaritons to a system with structured upper and lower polariton curves. For an incident angle of 49°, (Vasa *et al.*, 2010) demonstrates that a pump pulse can significantly lower the reflectivity of the system by activating the reflection minima in these structured curves.

Active control of the strong coupling regime is also demonstrated in (Berrier *et al.*, 2011) by a much different means. An ATR setup is used in which light is coupled to SPP waves on the output side of a metal film (which is covered with emitters) via a prism. The oscillator strength of the emitters is controlled by introducing nitrogen dioxide into the system. As the concentration is increased from 0 PPM to 6 PPM, the dispersion changes from an uncoupled SPP wave to that of a hybrid system; avoided crossing is observed with a corresponding Rabi splitting of 130 meV. A coherent energy exchange develops in which "light and matter exchange energy for a certain number of periods before the energy escapes the system" (Berrier *et al.*, 2011). The system can be uncoupled by heating the sample, causing the reflectance spectrum to

display a single ATR minimum instead of two.

Changes in the optical properties of a hybrid material from an ultrashort laser pulse are observed in simulations performed by Sukharev *et al.* (2013). The simulations demonstrate that the coherent energy exchange between emitters and SPPs occurs over femtoseconds and this time scale can be adjusted via material or laser parameters.

The Rabi oscillations are observed by pumping the emitters and then sending in a probe pulse after a delay time $\Delta\tau$, with $\Delta\tau = 0$ corresponding to the probe pulse being sent right as the pump pulse begins. This is clearly different from simply probing the system, as a much larger number of emitters are excited. A series of simulations is run, each with a longer $\Delta\tau$. Running this sequence of simulations maps out the effect of the pump pulse over time; the Rabi oscillations are clearly seen in a plot of reflectance (R) vs. time (Fig. 1.4).

For a 15 fs pump, a graph of pump delay $\Delta\tau$ versus change in reflectance ΔR shows that ΔR increases for the upper and lower polaritons relative to their values without any pumping. This is thought to be caused by energy transfer between the SPPs and the emitters: the period of oscillations in the ΔR vs $\Delta\tau$ graph is 3.75 fs and this time depends only upon the local electric field strength and the emitter dipole moment. It does not vary appreciably when slit period or emitter density is changed. This period of oscillation does depend on the peak pump amplitude. For a 30 fs pump pulse that is resonant with the emitters, ΔR vs. $\Delta\tau$ is plotted for two different peak pump amplitudes. At 2×10^9 V/m, the period of oscillation is 3 fs and at 4×10^9 V/m the period of oscillation is 6 fs (see Fig. 1.4). Two surprising results are also observed: the Rabi period slows down over time and the Rabi frequency is smaller in these simulations as compared to a simple two-level atom in the same laser field.
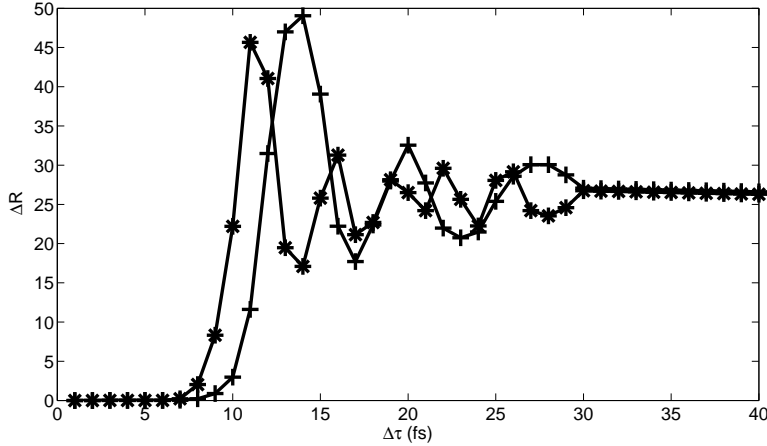
Figure 1.4: Femtosecond oscillations of ΔR. The raw data is taken from Sukharev *et al.* (2013) The Rabi oscillation period depends on the pump amplitude. $+$ symbols indicate an amplitude of 2×10^9 V/m (the oscillation period is 6 fs) and $*$ symbols indicate an amplitude of 4×10^9 V/m (the oscillation period is 3 fs).

A longer (180 fs) pump pulse is used to map out the excitation dynamics. The oscillations of ΔR and those of the ground state population are in step with one another, suggesting that the oscillations in the transient spectra are caused by transitions of the emitters between the ground state and the excited state.

Additionally, a pump pulse is applied and then abruptly truncated to zero. This is a promising means of controlling the number of Rabi oscillations. With this in mind, one could conceivably manipulate the time envelope and the incident angle of the pump pulse to control the plasmon energy distribution.

Another instance of optical control of energy distribution in hybrid materials is in Sukharev (2014). The transmission coefficient is able to be modified by using two different types of emitters each with different resonant energies. These emitters are coupled to a silver sinusoidal grating. Two absorption features are present in the bare grating and they are identified as SPPs by noting that the minima in the transmission spectrum correspond to the maxima in the reflection spectrum. The fields of the SPPs are very inhomogeneous, and the spatial distribution of fields reveals the spatial extent

17

of the coupling for each type of emitter.

The SPP resonances are able to be swept across the emitter resonances by varying the amplitude of the grating. When the two types of emitters are added, the lower energy resonance is seen to undergo Rabi splitting as would be expected. The higher energy resonance not only undergoes splitting, but (for an amplitude of 60 nm and greater) exhibits the collective peak that was previously described. The density and dipole moment are not particularly large, but the fields (which of course affect coupling) associated with this higher energy are much larger, giving rise to the collective peak.

A chirped laser pulse (in this case, a pulse whose frequency increases or decreases linearly over time) can be used to selectively excite either one emitter type or the other, which was verified by sending a pulse into a single emitter only and recording the density matrix elements corresponding to the ground and excited states. If the laser pulse starts at the frequency of higher energy emitters and decreases, the lower-energy emitters will be excited and the higher-energy type will not be; and vice versa for the laser pulse starting at the lower emitter frequency and increasing. Given that the two types of emitters couple to different SPP modes, whose fields corresponding to each mode have different spatial distributions, a positive chirp will excite one set of regions and a negative chirp will excite a different set of regions. These chirped pulses effectively pump one type of emitter, causing its response to a subsequent probe pulse to differ from that without the chirped pulse.

As is shown in Fig. 1.5, the transmission at the lower SPP resonance is altered by a negative chirp (but not much by a positive chirp) and transmission at the higher SPP resonance is altered by a positive chirp (but not much by a negative chirp). The simulations show that a negative chirp inverts the lower energy emitters whereas a positive chirp causes the higher energy emitters to undergo several Rabi oscillations.

18
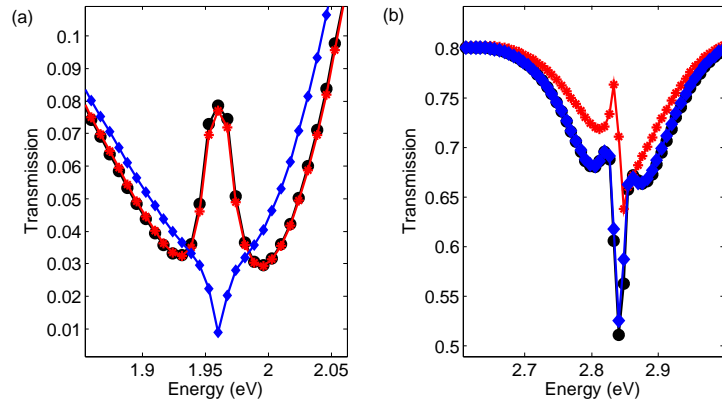
Figure 1.5: Panel (a) shows the lower polariton and panel (b) shows the upper polariton. Raw data taken from Sukharev (2014). Circles indicate no chirp, diamonds indicate a negative chirp, and asterisks indicate a positive chirp. A negative chirp alters the lower polariton whereas a positive chirp does not. A positive chirp alters the upper polariton whereas a negative chirp has no effect on it.

Chapter 2

MODELING THE INTERACTION OF LIGHT AND MATTER AT THE MICROSCOPIC SCALE

The interaction of light with nanoscale plasmonic structures must account for the classical behavior of both light and metal as well as the quantum behavior of emitters. The structures considered here consist of either an ensemble of emitters, a silver structure, or are hybrid (silver plus quantum emitters). Silver is optimal for plasmonic applications because its parameters are well suited to SPP features in the visible range, e.g. no interband transitions in this region (LeRu and Etchegoin, 2009).

2.1 The Finite Difference Time Domain (FDTD) Method

Maxwell's equations are used to describe the propagation of electromagnetic waves:

$$\mu_0 \frac{\partial \vec{H}}{\partial t} = -\nabla \times \vec{E} \tag{2.1a}$$

$$\epsilon_0 \frac{\partial \vec{E}}{\partial t} = \nabla \times \vec{H} - \vec{J} \tag{2.1b}$$

μ_0 is the permeability of free space (we assume that the relative magnetic permeability is 1.0), ϵ_0 is the permttivity of free space, $\vec{E}$ is the electric field, $\vec{H}$ is the magnetic field and $\vec{J}$ is the current density.

Maxwell's equations are of course continuous partial differential equations with a limited number of analytical solutions. One cannot hope to find analytical solutions that account for arbitrary geometries with dispersive structures and quantum emitters. We therefore discretize the system by evaluating derivatives at finite distances and time steps apart. For instance, a spatial derivative of the y-component of the

20

E-field becomes:

$$\frac{\partial E_y}{\partial x} \rightarrow \frac{E_y(i+1,j) - E_y(i,j)}{dx} \qquad (2.2)$$

The indices i and j indicate grid points at which the fields are evaluated. Given that this is an approximation to the correct physics, one must take steps to ensure the accuracy of the results. The most reassuring procedure is to decrease the spatial resolution incrementally and verify convergence. When the results no longer change with decreasing spatial step size, the simulation is converged.

Several methods exist for discretizing and propagating Maxwell's equations. The method used in this research is the finite difference time domain (FDTD) method (Taflove and Hagness, 2005), introduced by Yee in 1966 (Yee, 1966). The mesh consists of two shifted grids: one for the electric field and one for the magnetic field. In three dimensions, each E-field vector is surrounded by four H-field vectors and vice versa; this makes evaluation of $\nabla \times \vec{E}$ and $\nabla \times \vec{H}$ very straightforward. All of the results presented herein that employ FDTD use either a one- or two-dimensional grid. In a one-dimensional grid, the structure is taken to be infinitely long in the x- and y-directions and the fields propagate along the z-direction. In a two-dimensional grid, the fields E_x, E_y and H_z are evaluated in the x-y plane and the structure is taken to be infinitely long in the z-direction. Thus, each H_z vector is calculated using four surrounding E-field vectors (two E_x and two E_y vectors) whereas each E-field vector is calculated using only two adjacent H_z values as the H_x and H_y values are zero everywhere, which must be so because there is no variation of any of the fields along z. The H-field vectors point along z whereas the E-field vector has x and y components. This corresponds to p-polarization (E-field in the plane of incidence); s-polarization (E-field perpendicular to the plane of incidence) cannot excite SPPs.

A total-field / scattered-field (TFSF) formulation is used to introduce a plane wave

into the grid. This is consistent with the illumination of a small sample with a beam that covers all of it as well as the periodic nature of the structure. A lookup table (Taflove and Hagness, 2005) is used to project the values of E and H onto the TFSF boundary, and this generates the incident wave. While the physical system is open, it makes sense to terminate it in regions sufficiently far from the structure. This is accomplished by adding absorbing boundaries which are implemented as *convolutional perfectly matched layers* (CPML). For periodic structures, CPML is added to the top and bottom of the grid while a periodic boundary condition is applied to the left and right of the grid.

2.2   Metal and Emitters

The Drude model (LeRu and Etchegoin, 2009) is used to describe the dispersion of the metal. An electron cloud that is bound to an atom is treated as a damped harmonic oscillator with resonant frequency ω_0. Its motion is solved for, and then $\omega_0 = 0$ is assumed yielding the frequency-dependent dielectric constant:

$$\epsilon(\omega) = \epsilon_r - \frac{\omega_p^2}{\omega^2 - i\gamma\omega} \tag{2.3}$$

ω_p is the plasma frequency (i.e. the natural frequency of the free electron plasma), γ is the damping that corresponds to collisions between the free electrons and the crystal (LeRu and Etchegoin, 2009), and ϵ_r is the high-frequency limit of the dielectric function (Sukharev, 2012). For silver, these values are 1.76×10^{16} rad/s, 3.08×10^{14} rad/s, and 8.26 respectively (Gray and Kupka, 2003). In metal, the field values (obtained from the Maxwell equations) are used to update the currents (Gray and Kupka, 2003):

$$\frac{\partial \vec{J}}{\partial t} = -\gamma \vec{J} + \epsilon_0 \omega_p^2 \vec{E} \tag{2.4}$$

The case where $\omega_0 \neq 0$ is also of interest, as this leads to the classical model of polarization. We will characterize the susceptibility of the two-level emitters in this context. The susceptibility in this case is given by:

$$\chi(\omega) = \frac{\epsilon(\omega)}{\epsilon_0} - 1 = \frac{Ne^2}{\epsilon_0 m} \sum_j f_j (\omega_j^2 - \omega^2 - i\omega\gamma_j)^{-1} \tag{2.5}$$

N is the number of molecules per unit volume, $\epsilon(\omega)$ is the permittivity at a given frequency, and f_j is the number of electrons per molecule with binding frequency ω_j and damping γ_j. Near a resonance ($\omega = \omega_j$), the real part of χ undergoes anomalous dispersion while the imaginary part undergoes resonant absorption.

2.3   Maxwell-Bloch Equations and Two-Level Emitters

2.3.1   Density Matrix Formulation

The Schrodinger equation describes the evolution of a wavefunction in time. An equivalent formulation uses the *density matrix*, whose dynamics are described by the Liouville-von Neumann equation (discussed in the next section). The density matrix formulation accounts for the observer possibly not knowing the exact state of the system. This is known as a *mixed state*, as opposed to a *pure state*. A *partially mixed state* is a state in which interference effects are present but reduced (MSU, 2009).

When we deal with an ensemble of particles, it could be that every state of every particle is known. This corresponds to a pure state (additionally, any linear combination of pure states is also a pure state). On the other hand, it may be that the states of the particles are only known statistically (say, 25% in one state and 75% in another). This corresponds to a mixed state, and the probability for the particle to be in one state or another is classical (i.e. it does not derive from a probability amplitude, which of course creates interference effects (MSU, 2009)).

23

Following MSU (2009), consider a beam of silver atoms in a Stern-Gerlach experiment, with each atom described by the following pure state (which happens to be $|+x\rangle$ expressed in the z basis):

$$|A\rangle = \frac{1}{\sqrt{2}}(|\uparrow\rangle + |\downarrow\rangle)$$

And consider another separate beam with 50% of the atoms in the state $|\uparrow\rangle$ and the other 50% in the state $|\downarrow\rangle$:

$$|B\rangle = 50\% \, |\uparrow\rangle \text{ and } 50\% \, |\downarrow\rangle$$

One can actually distinguish these two beams experimentally. Measuring the z-component of spin for each beam will give the identical result of half up and half down. Measuring the x-component of spin, however, yields $|+x\rangle$ every time for Beam A:

$$\langle +x|A\rangle = \langle +x|+x\rangle = 1$$
$$\langle -x|A\rangle = \langle -x|+x\rangle = 0$$
$$P_{A,+x} = |\langle +x|A\rangle|^2 = 1$$
$$P_{A,-x} = |\langle -x|A\rangle|^2 = 0$$

For the mixed state B, a measurement of the x-component yields $|+x\rangle$ half the time and $|-x\rangle$ half the time. Calculating the coefficients $\langle +x|+z\rangle$ and $\langle +x|-z\rangle$:

$$\langle +x|+z\rangle = \frac{1}{\sqrt{2}}(\langle +z| + \langle -z|)\,|+z\rangle = \frac{1}{\sqrt{2}}$$
$$\langle +x|-z\rangle = \frac{1}{\sqrt{2}}(\langle +z| + \langle -z|)\,|-z\rangle = \frac{1}{\sqrt{2}},$$

24

which yields the following probability of observing $|+x\rangle$:

$$P_{B,+x} = \frac{1}{2}|\langle +x|+z\rangle|^2 + \frac{1}{2}|\langle +x|-z\rangle|^2 = \frac{1}{2}$$

Calculating the coefficients of $\langle -x|+z\rangle$ and $\langle -x|-z\rangle$:

$$\langle -x|+z\rangle = \frac{1}{\sqrt{2}}(\langle +z| - \langle -z|)\,|+z\rangle = \frac{1}{\sqrt{2}}$$

$$\langle -x|-z\rangle = \frac{1}{\sqrt{2}}(\langle +z| - \langle -z|)\,|-z\rangle = \frac{1}{\sqrt{2}},$$

which yields the following probability of observing $|-x\rangle$:

$$P_{B,-x} = \frac{1}{2}(|\langle -x|+z\rangle|^2 + |\langle -x|-z\rangle|^2) = \frac{1}{2}$$

We can use the density matrix operator to handle mixed states where the ith state has probability P_i:

$$\hat{\rho} = \Sigma_i P_i\,|\psi_i\rangle\,\langle\psi_i| \tag{2.6}$$

We specify an orthonormal basis to obtain the matrix elements. The matrix element ρ_{jk} is obtained as follows:

$$\langle j|\,\hat{\rho}\,|k\rangle$$

$$= \langle j|\,\Sigma_i P_i\,|\psi_i\rangle\,\langle\psi_i|\,|k\rangle$$

$$= \Sigma_i P_i\,\langle j|\psi_i\rangle\,\langle\psi_i|k\rangle$$

The matrix element ρ_{jj} is then:

$$\langle j| \hat{\rho} |j\rangle = \Sigma_i P_i \langle j|\psi_i\rangle \langle\psi_i|j\rangle$$

$$= \Sigma_i P_i| \langle\psi_i|j\rangle |^2,$$

which is the probability of observing the state $|j\rangle$. Hence, given an ensemble of particles, the diagonal elements ρ_{jj} of the density matrix represent the population in the given state j. The off-diagonal elements are an average of the cross terms $\langle j|\psi_i\rangle \langle\psi_i|k\rangle$ over each and every pure state ψ_i that comprises the mixed state. These elements represent coherence, that is, interference between two given states j and k. For a two-level emitter, the macroscopic dipole moment is proportional to the off-diagonal elements of the density matrix (Tang, 1979). The macroscopic polarization consists of the sum of the individual atomic dipole moments, so it must depend on the coherence of the individual dipoles (Tang, 1979).

The expectation value of an operator $\hat{A}$ is conveniently calculated by:

$$< \hat{A} >= Tr(\hat{\rho}\hat{A}) \tag{2.7}$$

And the time dynamics of the density matrix are described by the Liouville von Neumann equation, which is derived as follows:

$$\frac{d\hat{\rho}}{dt} = \frac{d |\psi\rangle}{dt} \langle\psi| + |\psi\rangle \frac{d \langle\psi|}{dt}$$

The Schrodinger equation $H\psi = i\hbar\frac{\partial\psi}{\partial t}$ is invoked:

$$= -\frac{i}{\hbar}H |\psi\rangle \langle\psi| + \frac{i}{\hbar} |\psi\rangle \langle\psi| H,$$

which leads to the *Liouville-von Neumann equation*:

$$\frac{d\hat{\rho}}{dt} = -\frac{i}{\hbar}[\hat{H}, \hat{\rho}] \tag{2.8}$$

26

Damping is accounted for as follows:

$$\frac{d\hat{\rho}}{dt} = -\frac{i}{\hbar}[\hat{H}, \hat{\rho}] - \hat{\Gamma}\hat{\rho} \tag{2.9}$$

Interatomic interactions are absent from this approach, so we could theoretically use the Schrodinger equation to describe the state of each atom. But practically speaking, we would be unable to include damping and we would be restricted to delta function potentials describing a transition with infinitely narrow width. We therefore proceed with the density matrix formulation, as it lends itself to straightforward calculation of populations in different energy states and permits a simple means of including damping.

2.3.2 Quantum Dynamics

The Liouville-von Neumann equation (Eq. 2.9) is used to describe the time dependence of an atom interacting with an electromagnetic field. The Hamiltonian $\hat{H}$ describes an atom with dipole moment $\vec{\mu}$ interacting with an electric field:

$$\hat{H} = \hat{H}_0 - \hat{\vec{\mu}} \cdot \vec{E}(t) \tag{2.10}$$

The majority of the work is carried out in two dimensions with p-polarized fields. As demonstrated previously, it is necessary to choose a basis in order to form the density matrix elements. With an eye toward complex, multi-level systems, the basis chosen for two-dimensional systems in this work consists of hydrogen atom states: $|1\rangle = |s\rangle$, $|2\rangle = (|p_x\rangle + i|p_y\rangle)/\sqrt{2}$, $|3\rangle = (|p_x\rangle - i|p_y\rangle)/\sqrt{2}$. (One-dimensional systems follow similarly but are simpler and will not be described here.)

It is also necessary to obtain the matrix elements of the Hamiltonian from the operator 2.10, and to do so we express it in the aforementioned basis. The diagonal elements correspond to the energy relative to $|1\rangle$ (so $H_{11} = 0$ and $H_{22} = H_{33} = \hbar\omega_a$,

27

where $\hbar\omega_a$ is the transition energy between $|1\rangle$ and either of the degenerate states).

As an example, we expand the element H_{22}:

$$\langle 2| (\hat{H}_0 - \hat{\vec{\mu}} \cdot \vec{E}(t)) |2\rangle$$

$$= \langle 2| \hat{H}_0 |2\rangle - \langle 2| \hat{\vec{\mu}} \cdot \vec{E}(t) |2\rangle$$

$$= \hbar\omega_a - \int \Psi^*_{211}(q\hat{\vec{r}} \cdot \vec{E})\Psi_{211} d^3r$$

$$= \hbar\omega_a - q \int \Psi^*_{211}(xE_x + yE_y)\Psi_{211} d^3r$$

The integral involves integrals over spherical harmonics, which evaluate to zero for H_{22}. That is not always the case for the off-diagonal elements, which involve calculation of transition dipole moments.

Expanding the Hamiltonian in matrix form yields:

$$\begin{bmatrix} 0 & \Omega_-(t) & -\Omega_+(t) \\ \Omega_+(t) & \hbar\omega_a & 0 \\ -\Omega_-(t) & 0 & \hbar\omega_a \end{bmatrix} \tag{2.11}$$

$\Omega_\pm = \mu_{sp}[E_x(t) \pm iE_y(t)]/\sqrt{6}$, $\hbar\omega_a$ is the transition energy, and μ_{sp} is the s-p matrix element of the dipole moment operator (Sukharev and Nitzan, 2011). The matrix is not diagonal as we are not using a basis of energy eigenstates, and thus the Liouville-von Neumann equation will yield off-diagonal elements for the density matrix.

According to Eq. 2.10:

$$\hat{\mu}_x = -\frac{\partial\hat{H}}{\partial E_x} = \frac{\mu_{sp}}{\sqrt{6}} \begin{bmatrix} 0 & -1 & 1 \\ -1 & 0 & 0 \\ 1 & 0 & 0 \end{bmatrix} \tag{2.12}$$

and

$$\hat{\mu}_y = -\frac{\partial \hat{H}}{\partial E_y} = \frac{\mu_{sp}}{\sqrt{6}} \begin{bmatrix} 0 & i & i \\ -i & 0 & 0 \\ -i & 0 & 0 \end{bmatrix} \tag{2.13}$$

Eq. 2.11 is combined with Eq. 2.9 to yield the density matrix elements:

$$\frac{d\rho_{11}}{dt} = i\omega_+(\rho_{12} + \rho_{13}^*) - i\omega_-(\rho_{13} + \rho_{12}^*) + \gamma_1(\rho_{22} + \rho_{33})$$

$$\frac{d\rho_{12}}{dt} = i\omega_a\rho_{12} - i\omega_-(\rho_{22} - \rho_{11}) + i\omega_+\rho_{23}^* - \gamma_2\rho_{12}$$

$$\frac{d\rho_{13}}{dt} = i\omega_a\rho_{13} + i\omega_+(\rho_{33} - \rho_{11}) - i\omega_-\rho_{23} - \gamma_2\rho_{13}$$

$$\frac{d\rho_{22}}{dt} = i\omega_-\rho_{12}^* - i\omega_+\rho_{12} - \gamma_1\rho_{22}$$

$$\frac{d\rho_{23}}{dt} = -i\omega_+(\rho_{13} + \rho_{12}^*) - 2\gamma_2\rho_{23}$$

$$\frac{d\rho_{33}}{dt} = i\omega_-\rho_{13} - i\omega_+\rho_{13}^* - \gamma_1\rho_{33}$$

$\omega_\pm = \Omega_\pm/\hbar$ and $\gamma_2 = \gamma_p + \gamma_1/2$, where γ_p represents pure dephasing (Sukharev and Nitzan, 2011).

In regions containing emitters, the fields are used to update the density matrix elements via the Liouville-von Neumann equation. The expectation value of the dipole moment operator is obtained by taking the trace of the product of the dipole moment operator and the density matrix:

$$< \vec{\mu} > = Tr(\hat{\rho}\hat{\mu}) \tag{2.14}$$

The updated expectation value of the dipole moment is used to calculate the volume polarization and then the polarization current of the emitters, which is subsequently
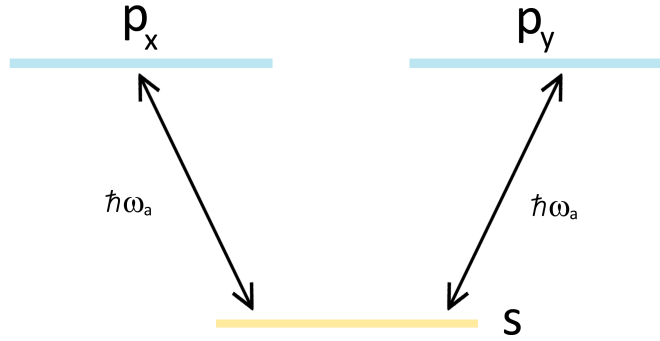
Figure 2.1: Energy level diagram for emitters. The ground state is an s-type state and the excited state consists of two p-type states.

inserted into the Ampere-Maxwell Law:

$$\vec{P} = n_a < \vec{\mu} > \tag{2.15a}$$

$$\vec{J}_p = \frac{\partial \vec{P}}{\partial t} \tag{2.15b}$$

n_a is the volume density of emitters, $\vec{P}$ is the polarization per unit volume, and $\vec{J}_p$ is the polarization current.

The approach is self-consistent in that all of the physics is described by the aforementioned equations, with each equation getting all that it requires entirely from the other equations.

2.4 Excitation and Detection

In the linear regime, when the frequency response of a system to external EM excitation is independent from the excitation intensity, one can use a short pulse

method to obtain the spectrum of the system within a single FDTD run (Sukharev and Nitzan, 2011) rather than running a series of simulations with CW waves of different frequencies. The reflection and / or transmission spectra are calculated by launching a short pulse whose duration is on the order of femtoseconds at the structure. The form of the pulse is such that its value is zero at t = 0 and t = τ and its derivative is zero at those times which is important for numerical convergence. (One example is $E_0 \sin^2(\frac{\pi t}{\tau}) \cos(\omega t)$.) The Poynting vector is formed by the cross product of the Fourier transformed E- and H-fields (in runs with two dimensions, $E_x H_z$). To obtain reflection spectra, this calculation is performed in the scattered-field region, thereby measuring only the reflected fields. The transmission spectrum is calculated in the total-field region. In two dimensions, the y-component of the Poynting vector is spatially integrated across the grid.

A digital Fourier transform (DFT) (Taflove and Hagness, 2005) is used to integrate the Poynting vector across the unit cell. This method multiplies the fields by phasor functions at each time step. Because the fields are transformed on-the-fly, this method requires much less memory than recording the fields at every point and transforming at the end, which requires an array at every point of interest whose size is equal to the (usually large) number of time steps. Thus, the slight performance penalty incurred by using DFT is more than compensated for as it allows the inclusion of more grid points in calculating integrated energy flux.

31

Chapter 3

PERIODIC HYBRID MATERIALS AT OBLIQUE INCIDENCE

3.1   Oblique Incidence

It is very useful to be able to tilt the incoming wave. Infinite, repeating structures are modeled and therefore periodic boundary conditions (PBCs) are imposed on a single unit cell. When PBCs are combined with obliquely incident waves, the numerical situation becomes much more involved than one might expect. The work presented in this chapter was published in Blake and Sukharev (2015a).

For normal incidence, the PBC can be applied by simply using fields from one boundary to calculate fields at the other. For oblique incidence, however, one can see from Fig. 3.1 that the fields on the right boundary are equal to those on the left boundary at a time t_{delay} in the past. Applying the PBC at the right boundary is straightforward: the field values at the left boundary are recorded and applied at a time t_{delay} later. Matching the left boundary to the right, however, requires that we know the fields at a time t_{delay} in the future which of course is not possible. Several methods (spectral FDTD (Aminian and Rahmat-Samii, 2006), sin/cos (Harms and Mittra, 1994), multiple unit cells (Taflove and Hagness, 2005), etc.) have been developed to reconcile this issue, though many were cumbersome (sin/cos) or came with excessive computing times (multiple unit cell).

A method developed by Todd Lee is both robust and straightforward (Lee and Smith, 2005). The grid is broken up into two unit cells as shown in Fig. 3.1. The fields in the good cell (on the right) are always accurate whereas the fields in the bad cell (on the left) are subject to an error that fills the cell over time. Rather
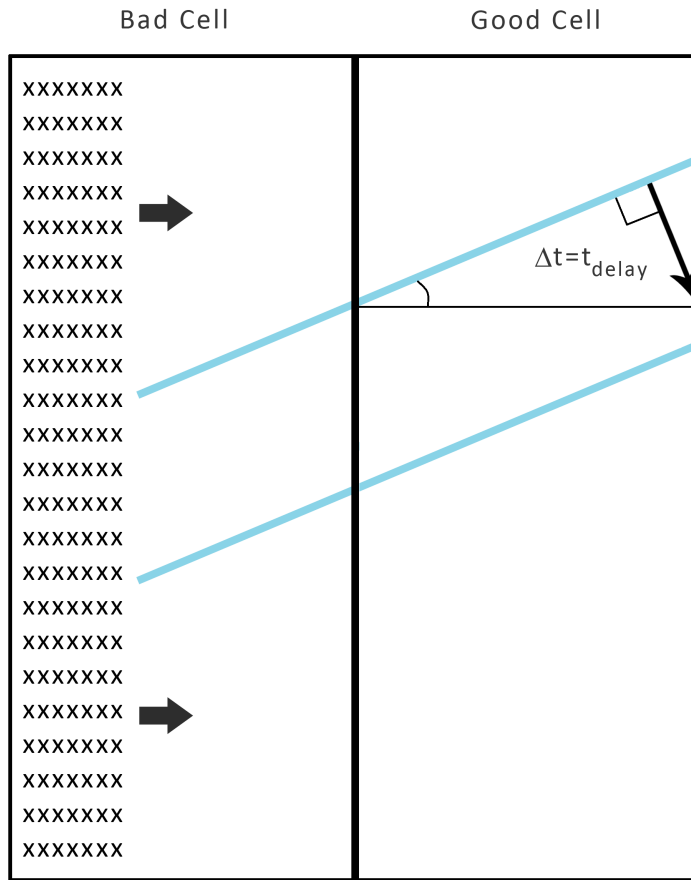
Figure 3.1: Error propagation and delay time in applying periodic boundary conditions. The error propagates from the left boundary of the bad cell at the speed of light in that medium. The periodic boundary condition is enforced on the left and right boundaries of the good cell.

than enforce a PBC or an absorbing boundary on the left side of the bad cell, it is simply left to propagate with a value of zero to the left of it. This causes an error that propagates from the boundary at the speed of light, but the critical point is that the wave reaches the right unit cell before the error does for $\theta_{inc} < 90°$. The wave

propagates into the rightmost unit cell and is allowed to continue propagating until the error from the left boundary reaches the rightmost unit cell. At that point, the values in the right unit cell (which are still valid) are copied into the left unit cell, and the right unit cell gets values pasted into it from a previous time step. This ensures that there is no discontinuity in the wavefront. The process is allowed to run until the error again reaches the right unit cell.

We tested this method thoroughly. The electric field updates properly and is absorbed by the CPML boundaries, as expected. The simulation has been stable for every geometry modeled and every angle of wave (up to and excluding 90°).

To test the method, a dispersionless dielectric (n = 1.414) is placed on the lower half of the grid and vacuum (n = 1.0) on the upper half. The reflection (R) and transmission (T) values, which are derived from the Fresnel equations, were compared with analytical values given by Griffiths (1998):

$$\alpha = \frac{\sqrt{1 - [\frac{n_1}{n_2} sin\theta_i]^2}}{cos\theta_i} \tag{3.1a}$$

$$\beta = \frac{n_2}{n_1} \tag{3.1b}$$

$$T = \alpha\beta(\frac{2}{\alpha + \beta})^2 \tag{3.1c}$$

$$R = (\frac{\alpha - \beta}{\alpha + \beta})^2 \tag{3.1d}$$

The results are shown in Fig. 3.2. The simulations were run with a spatial step of 1.0 nm and for 300,000 time steps, which corresponds to a time of 500 fs. The agreement between theory and the simulations is excellent.

The transmittance and reflectance were found to be identical at different frequencies, which is expected given that this setup is dispersionless. Also, these values remained constant as the grid was widened and / or lengthened. Additionally, the

34
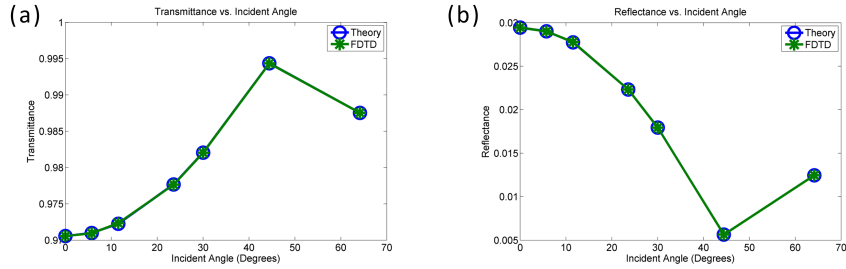
Figure 3.2: Comparison of analytical transmittance and reflectance showing accurate results obtained from FDTD. a) Transmittance. b) Reflectance.

angles of reflection and refraction were found to behave as expected. The maximum in the T graph and the minimum in the R graph correspond to a Brewster angle.

These comparisons with well-established but non-trivial theory give confidence that the code is working correctly.

3.2 Problems with Critical Angle and Total Internal Reflection

Unfortunately, problems arise in using this copy/shift routine when one tries to simulate total internal reflection (TIR). For this discussion, the top half of the grid (region 1) will have n_1 and the bottom half (region 2) will have n_2 where $n_1 > n_2$. As stated previously, the copy/shift routine assumes that an error travels from the left boundary of the bad cell to the left boundary of the good cell in a time t_{error}, which must be greater than the time t_{delay} it takes for the periodic time to be reached. As will be shown here, when the wave is launched from n_1 to n_2 at the critical angle or greater, t_{delay} is equal to or greater than t_{error}. In other words, once the time t_{delay} is reached, the error has already propagated into the good unit cell. The simulation must run for at least t_{delay} for the copying and shifting to take place and will therefore not work under these conditions.

Specifically, t_{error} is the least amount of time it takes for the error to propagate from the edge of the bad cell up to the good cell. This time can vary if different regions of the grid have different indices of refraction. The entire grid is copied and shifted at the same time, and this happens when the error reaches the boundary of the good cell. In the region with the lower index of refraction, we have $v_2 = c/n_2$ which is greater than $v_1 = c/n_1$. Because the error travels faster in region 2, the time that it takes for the error to reach the boundary in region 2 is used to calculate t_{error}:

$$t_{error} = \frac{unit\ cell\ width}{v_2} = \frac{unit\ cell\ width}{\left(\frac{c}{n_2}\right)} = \frac{n_2 \times unit\ cell\ width}{c} \qquad (3.2)$$

The simulation must run for at least the region 1 delay time t_{delay} so that the copy/shift routine can take place. First, it is shown that the delay time in region 1 is equal to that of region 2. The delay time in region 1 is:

$$t_{delay1} = \frac{unit\ cell\ width \times sin\theta_1}{v_1} = \frac{n_1 \times unit\ cell\ width \times sin\theta_1}{c} \qquad (3.3)$$

And the delay time in region 2 is:

$$t_{delay2} = \frac{unit\ cell\ width \times sin\theta_2}{v_2} = \frac{n_2 \times unit\ cell\ width \times sin\theta_2}{c} \qquad (3.4)$$

By Snells Law, $n_1 sin\theta_1 = n_2 sin\theta_2$ so the delay times are equal. If they were not equal, this scheme would not work!

If the incident wave is launched from region 1 at the critical angle θ_c (so that by Snells Law, $sin\theta_c = \frac{n_2}{n_1}$), then the delay time becomes:

$$t_{delay1} = \frac{n_1 \times unit\ cell\ width \times sin\theta_c}{c} = \frac{n_1 \times unit\ cell\ width \times \frac{n_2}{n_1}}{c}$$
$$= \frac{n_2 \times unit\ cell\ width}{c} = t_{error}$$

And of course, any angle greater than the critical angle gives an even longer delay time. So any angle below the critical angle works fine and any angle equal to or greater than the critical angle will not work.

If one wishes to simulate a flat film, the film can simply be terminated instead of having the PBC applied to it. Unwanted features that depend on the length of the film will be present and these can be minimized (and moved to longer wavelengths) by increasing the length of the film, leaving accurate results in the frequency region of interest.

3.3 Exploration and Characterization of Sinusoidal Grating With and Without Emitters

3.3.1 Bare Silver Gratings: Previous and Present Results

Plasmon-assisted tunneling of light through sinusoidal (corrugated) gratings is examined in Avrutsky *et al.* (2000). The phenomenon of extraordinary optical transmission (EOT) is well known in quantum optics and was first seen by shining light through a thin film with a periodic array of holes and observing that the fraction of light transmitted was greater than the fraction of the film covered in holes (Ebbesen *et al.*, 1998). It is shown in Treacy (1999) and Avrutsky *et al.* (2000) that a sinusoidal grating is not only capable of producing this effect, but able to do so with a transmission peak that is stronger and more narrow than that of a periodic array of holes. Transmission through thin films is also explored in Treacy (2002).

A sinusoidal grating of the form shown in Fig. 3.3 is studied. Such sinusoidal gratings are investigated by Sukharev *et al.* (2009) and Mu *et al.* (2010). An in-phase grating with single-ended excitation, a period of 410 nm, an amplitude of 28.8 nm and thickness 20 nm is simulated, where it is shown that the symmetry of the grating
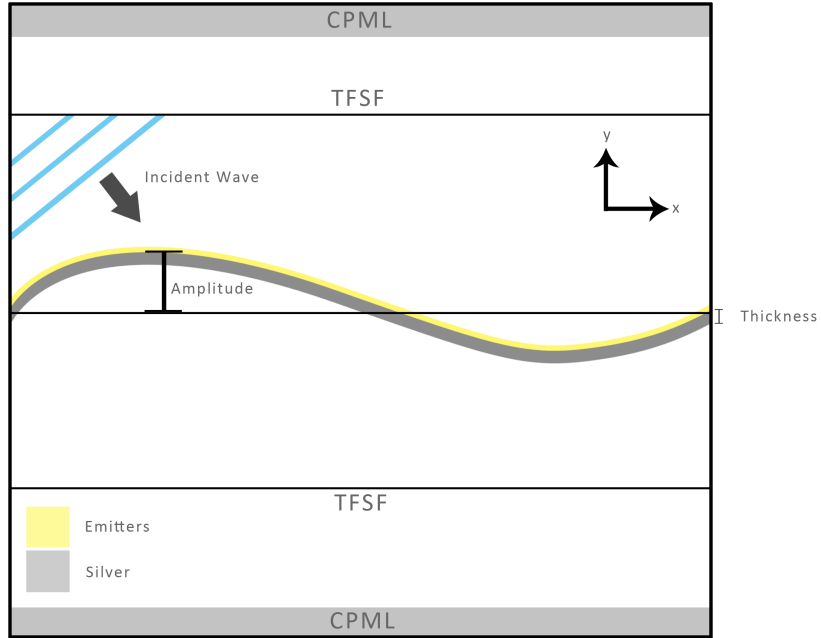
Figure 3.3: Schematic of silver / emitter hybrid sinusoidal system.

is such that the quantity T+R (rather than T or R separately) can be minimized for a single adjustable parameter, namely the grating amplitude. A graph of T + R from Sukharev *et al.* (2009) reveals a gently curved region at low wavelengths and SPP modes near 540 nm and 620 nm. Additionally, a Wood's anomaly is present at 532 nm (corresponding to a grating period of 400 nm and a refractive index of 1.33). This is a physical phenomenon that occurs when incoming and outgoing waves interact with waves that diffract tangent to the grating (Hessel and Oliner, 1965).

A sinusoidal grating with period 400 nm, amplitude 70 nm, and thickness 20 nm was run and the results are shown in Fig. 3.4. This spectrum, which compares well to that in Sukharev *et al.* (2009) is taken as a starting point for analyzing sinusoidal gratings. In addition to the two SPP modes seen in Fig. 3.4, a Wood's Anomaly is present at 3.1 eV. The energy of the Wood's anomaly is as expected for a 400 nm
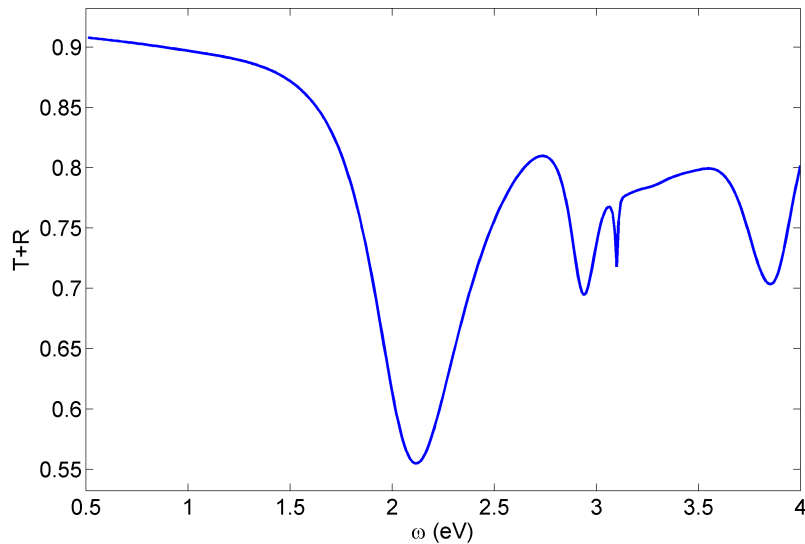
Figure 3.4: It is encouraging to see features corresponding to those in (Sukharev *et al.*, 2009): a gently curving region at low energies, a Wood's anomaly at 3.1 eV corresponding to n = 1.0 and a period of 400 nm, a broad resonance at lower energy and a narrow resonance at a higher energy. The simulation was run for 1×10^6 time steps (corresponding to a total time of 1.67×10^{-12} s). The spatial step size is 1.0 nm.

grating surrounded by a medium with a refractive index of 1.0, and it shifts to higher energies when the grating period is shortened.

The period, amplitude and thickness of the grating were adjusted. It was found that the previously mentioned period of 400 nm, amplitude of 70 nm and thickness of 20 nm give well-defined features and these parameters were therefore used for the simulations that followed.

As the incident wave is tilted it is expected that excitation of higher order Brillouin zones will cause both SPP features to split and that is precisely what is seen. A progression of T+R from 0 degrees to 10 degrees is shown in Fig. 3.5a and a contour plot from 0 to 40 degrees is shown in Fig. 3.5b.
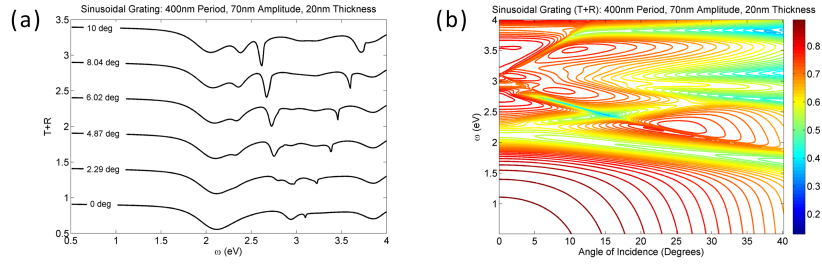
Figure 3.5: Spectra of the sinusoidal grating as the incident angle is varied. Amplitude is 70 nm, thickness is 20 nm and the period is 400 nm. a) The lower energy resonance (near 2.1 eV) begins to split at 2.29 degrees and this splitting clearly increases as the angle is increased. The higher energy resonance (near 2.9 eV) appears to have split at 2.29 degrees and the splitting becomes more pronounced as the incident angle is increased. At 10 degree incidence the higher energy resonance is beginning to overlap with the lower energy resonance. The Wood's anomaly moves to higher energies as expected. b) Contour plot showing the variation in the spectrum as incident angle is varied. The higher energy SPP mode crosses the (split) lower energy mode near an incident angle of 15 degrees. An observable avoided crossing might be expected if the coupling between these modes were to be increased.

3.3.2 Oblique Incidence with Hybrid Silver / Emitter System

When oscillators are coupled (in this case, the oscillators are the SPPs and the emitters), avoided crossing is expected in which the energies of the upper and lower polaritons approach each other and reach a minimum separation value (Torma and Barnes, 2015). In this case, the emitter resonance is placed at 2.7 eV and the angle is swept from 0 to 10 degrees. Tilting the incident wave causes the SPP resonance to split. This split resonance shifts as the incident wave is tilted, effectively sweeping it across the emitter resonance. Coupling between the split SPP resonance and the emitter resonance causes Rabi splitting into upper and lower polaritons and avoided crossing is clearly demonstrated in Fig. 3.6.

In other simulations, the value of the emitter resonance is simply changed and the simulation is run again. It must be emphasized that this is a different way of
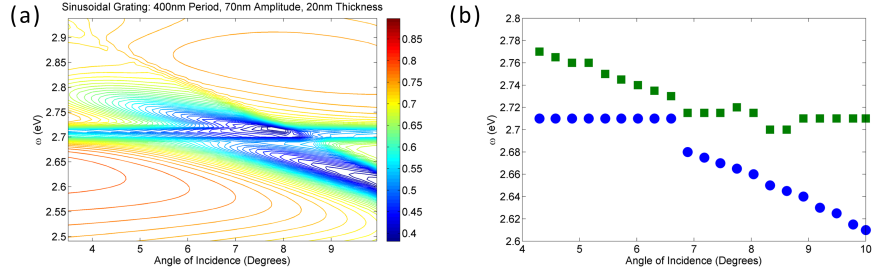
Figure 3.6: Avoided crossing is a signature of the strong coupling regime and is demonstrated here. a) Avoided crossing is observed when the incident wave is tilted, causing an SPP resonance to split and sweep past the emitter resonance. The quantity T+R is indicated by the contours. b) Upper polariton (squares) and lower polariton (circles) energies as a function of incident angle. The minimum energy separation is on the order of 20 meV.

observing avoided crossing: the incident wave is tilted such that an SPP resonance splits and as the incident wave is tilted further, this split resonance sweeps across the emitter resonance.

It is pointed out in Torma and Barnes (2015) that one of the attractions of the combination of having excitons as one of the oscillators and plasmon modes as the other is the very extensive control we have over the plasmon modes supported by metallic nanostructures. The geometry of the metallic structure can be adjusted to tune the SPP features as desired. In order to investigate strong coupling, one can prepare nanoscale slit arrays of varying periods with emitters deposited on top. This effectively sweeps the SPP resonance through the emitter resonance. The simulations performed in this work demonstrate the possibility of sweeping the SPP resonance much more efficiently: one can tilt the incident wave, causing an SPP resonance to split. As the incident wave is tilted, the split SPP feature sweeps past the emitter resonance, eliminating the need to use multiple nano-structures with different parameters.

41

Chapter 4

V-GROOVES

4.1   Introduction

The major point of interest in this section is to scrutinize the electromagnetic properties of molecular aggregates composed of simple two-level emitters strongly coupled to SPP waves supported by plasmonic waveguides. A periodic array of V-grooves was chosen as an example of such a waveguide. V-grooves are host to various optical phenomena, many of which involve the intense, highly localized fields that result from SPP waves. The work presented in this chapter was published in Blake and Sukharev (2015c).

Theoretical studies have been conducted using the Green's Function Integral Equation Method (Bhushan, 2012), yielding well-defined reflection features that are thought to result from surface plasmon polaritons, geometrical resonances, and a Wood's anomaly (Søndergaard and Bozhevolnyi, 2009). The origins of these features are identified by their response to changes in the geometry of the grooves: period, depth, groove angle, and angle of the incident fields. One point of interest is that one type of resonance displays intensity that is distributed over the entire groove whereas the intensity of another type is localized near the bottom of the groove.

A numerical investigation of how different SPPs interact with molecular aggregates in both linear and nonlinear regimes is conducted. The latter is considered using pump-probe simulations (Sukharev *et al.*, 2013). V-grooves offer two useful field distributions with which to investigate the strong coupling regime and it is beneficial to analyze unique phenomena such as the collective mode (discussed in Section 1.4,

referred to as the "third feature" in this section) in more than just one system, and hence with different configurations of fields, in order to characterize the phenomena more effectively. Additionally, we observe large Rabi splitting in the hybrid V-groove system, and we demonstrate that Rabi splitting can be eliminated with a femtosecond pump. The large Rabi splitting leads to substantial differences in the reflection spectrum compared to that of the uncoupled system, which suggests applications such as an optical switch.

4.2   Model

All of the results presented herein use a two-dimensional grid in which the fields E_x, E_y and H_z are evaluated in the x-y plane and the structure is taken to be infinitely long in the z-direction, as shown in Fig. 4.1. The fields are propagated via FDTD, the metal is described by the Drude model, and the time dynamics of the interaction between the EM field and the molecular aggregate is described by the Liouville-von Neumann equation.

The system under consideration is open in the y direction and periodic in x. We add absorbing boundaries using *convolutional perfectly matched layers* (CPML) on the top and the bottom of the grid as shown in Fig. 4.1. The left and right sides of the grid are terminated with periodic boundary conditions (PBCs) and the incident wave is introduced via a total field / scattered field (TFSF) approach (Taflove and Hagness, 2005). A spatial step of 1.0 nm was selected as results are converged for this spacing, which was demonstrated by obtaining the same data using a spatial size of 0.5 nm. A time step of $dx/(2c)$ was chosen such that the Courant stability condition is satisfied.

In the linear regime, when the frequency response of a system to external EM excitation is independent from the incident intensity, one can use a short pulse method
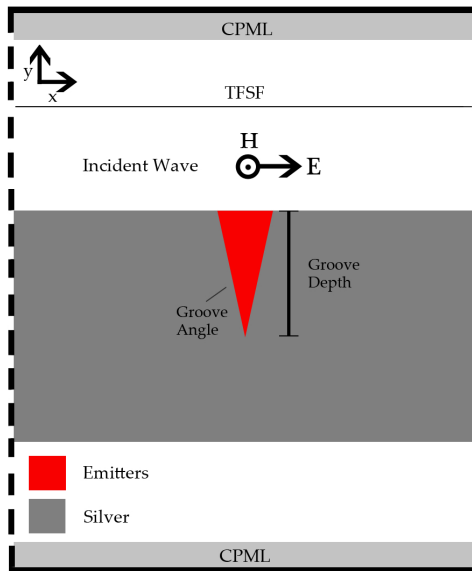
Figure 4.1: Schematic diagram of the system. The absorbing boundary conditions are implemented as *Convolutional Perfectly Matched Layers* (CPML). The periodic boundary conditions are imposed upon the left and right sides of the grid as indicated by the dashed lines. The incident wave is introduced via a *total-field / scattered-field* (TFSF) approach. The figure represents both the plane of incidence and the plane of scattering. The incident field is p-polarized and is normally incident on the grating as shown.

to obtain the spectrum of the system within a single FDTD run (Sukharev and Nitzan, 2011) as described earlier. Under the assumption that only the elastic scattering contributes to the spectrum, the reflection is calculated by launching a short pulse (of duration $\tau = 0.15 fs$ and whose form is $E_0 \sin^2(\frac{\pi t}{\tau}) \cos(\omega t)$) and spatially integrating the y-component of the Poynting vector (formed by the cross product of the Fourier transformed E- and H-fields; specifically, $E_x H_z$) along a line of constant y-value on the input side. This calculation is performed in the scattered-field region, thereby measuring only the reflected fields.

In order to account for all possible local field polarizations we consider quantum emitters with two energy levels, one of which is degenerate: an s-type ground state and two degenerate excited p-type states. In the basis of angular momentum, wave func-

44

tions are chosen (Sukharev and Nitzan, 2011): $|1\rangle = |s\rangle$, $|2\rangle = (|p_x\rangle + i\,|p_y\rangle)/\sqrt{2}$, $|3\rangle = (|p_x\rangle - i\,|p_y\rangle)/\sqrt{2}$.

The following set of parameters describing a quantum emitter is used in this paper: the transition dipole moment is 10 Debye and the radiationless lifetime of the excited state is 1 ps. The number density and the pure dephasing time are varied.

4.3   Results and discussion

The intent of this paper is to scrutinize the optical properties of a periodic system comprised of a periodic array of V-grooves in an optically thick silver film (the thickness of the film in all simulations is 800 nm) that is optically coupled to quantum emitters. We first consider a periodic array of V-grooves without emitters, followed by a hybrid system consisting of emitters (all starting in the ground state) added into the grooves, and finally this same system with an optical femtosecond pump applied.

The reflection spectrum of a bare silver grating with a 400 nm period obtained at normal incidence is shown in Fig. 4.2a. Three well-resolved resonances are observed with the energy of each depending on the geometrical parameters of the grating. Both of the resonances at lower energy are thought to be of a plasmonic, rather than geometrical, nature as each disappears when the conductivity of the metal is made infinite (i.e. perfectly reflecting by forcing the electric field to have a value of zero everywhere within the metal). The third resonance occurs at 3.09 eV, which corresponds to a wavelength of 401 nm. This is extremely close to the grating wavelength of 400 nm.

As noted in Søndergaard and Bozhevolnyi (2009), the intensity of the lower energy resonance is distributed throughout the groove whereas that of the higher energy resonance is localized near the bottom (see Fig. 4.2).

On account of each resonance being well-defined for this geometry, the remainder

45
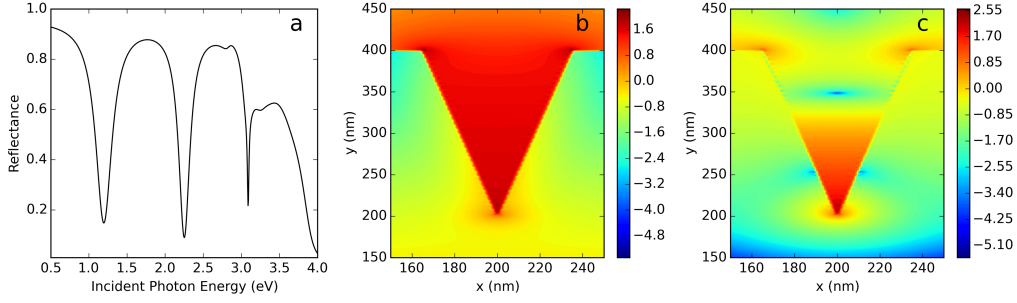
Figure 4.2: Linear optical response of bare V-grooves at normal incidence. Panel (a) shows reflection spectrum of bare grooves with 400 nm period, 20 degree groove angle and 200 nm groove depth. Panel (b) shows time-averaged intensity in the bare groove when excited by CW plane wave at 1.2 eV. The intensity is distributed throughout the groove. Panel (c) shows time-averaged intensity in the bare groove when excited with CW plane wave at 2.255 eV. The intensity is localized near the bottom of the groove. The contour data in panels (b) and (c) is logarithmic and normalized to the incident intensity.

of this work (unless otherwise specified) will focus on V-grooves with a period of 400 nm, a groove angle of 20 degrees, a groove depth of 200 nm, and normally incident fields.

We now consider the optical response of the system when emitters are added inside the grooves. When the emitters are resonant to the structure, normal mode splitting (Rabi splitting) is clearly observed (Fig. 4.3a). The Rabi splitting reaches 380 meV. This amount of splitting is considered large for hybrid nanostructures (Schlather *et al.*, 2013). Either at high emitter densities or a large transition dipole moment a third feature appears at or near the emitter resonance as can be seen in Fig. 4.3a near 1.2 eV. This feature, which is not predicted by the coupled-oscillator model, has been observed previously in simulations (Salomon *et al.*, 2012; Sukharev *et al.*, 2013; Antosiewicz *et al.*, 2014) as well as in experiments (Hutchison *et al.*, 2011; Salomon *et al.*, 2009; Sugawara *et al.*, 2006). Several observations discussed in Salomon *et al.* (2012) suggest that this peak has its origins in SPP enhanced emitter-emitter interactions.

To better understand the physics of this resonance we performed simulations gradually varying either groove angle (Fig. 4.3b) or groove depth (Fig. 4.3c). Note that the bare SPP lines plotted in Fig. 4.3b and 4.3c are clearly not linear with groove angle or groove depth (see below). By varying the groove depth or angle, we sweep the SPP resonance through the emitter's mode. In the reflection spectrum we record the energy positions of the lower and upper branch of the hybrid mode. This is carried out at the emitter density of 3×10^{26} emitters/m^3 (at which the third feature is prominent) and the results are shown in Fig. 4.3b and 4.3c. The results clearly indicate avoided crossing - an indication of the strong coupling due to efficient energy exchange between the corresponding SPP mode and molecular excitons (in our case these are simply two-level emitters). Next, the energy of the intermediate peak (green triangles in Fig. 4.3b and c) does not deviate appreciably from the emitter resonance even as the SPP resonance is tuned. Furthermore, this peak merges with the upper polariton as the thickness of a spacer layer between the grating and emitters increases. The dipole coupling between the emitters themselves is therefore suspected given the fall-off of this peak as the SPP field at the emitters' location decreases. Finally, a simulation was run in which the entire region containing emitters was replaced by a single two-level system (essentially a spatially distributed single emitter with a very large dipole moment), thereby eliminating any possible interaction between the emitters. In this case, the third peak disappears even under extremely high coupling conditions. This confirms earlier findings (Salomon *et al.*, 2012; Antosiewicz *et al.*, 2014) which suggested that the intermediate resonance located in the middle of the Rabi splitting corresponds to dipole-dipole interactions between emitters greatly enhanced by the SPP mode.

The strong coupling regime is defined in Torma and Barnes (2015) as when the coupling strength exceeds the linewidths of all damping processes and becomes exper-

imentally observable. In order to verify the onset of strong coupling, the dephasing time (and hence the linewidth of the emitter transition) was decreased from 400 fs to 5 fs over several increments. Even with the emitter resonance tuned to the SPP resonance (i.e. the strongest possible coupling), the Rabi splitting was not resolvable for dephasing times of 20 fs and lower.

The dashed lines in Fig. 4.3b and 4.3c are calculations of the values of the upper and lower polaritons using the coupled oscillator model. The coupled oscillator model has been shown in Salomon *et al.* (2012) to give accurate results so long as the coupling strength is not too high. The Hamiltonian of the coupled system is:

$$
\begin{bmatrix}
E_m & \Delta \\
\Delta & E_{pl}
\end{bmatrix}
\tag{4.1}
$$

E_{pl} is the SPP energy of the bare metallic grooves (obtained from simulations), E_m is the transition energy of uncoupled emitters, and 2Δ is the minimum Rabi splitting value. The eigenvalues obtained are:

$$
E_{U,L} = \frac{(E_{pl} + E_m) \pm \sqrt{(E_{pl} + E_m)^2 - 4\Delta^2}}{2}
\tag{4.2}
$$

$E_{U,L}$ are the energies of the upper or lower polaritons. In Fig. 4.3b, the comparison to the coupled oscillator model is close whereas in Fig. 4.3c it deviates somewhat at larger groove depths. In particular, we note that both the upper and lower polaritons appear to be "pinched" toward each other in Fig. 4.3c. We offer two possible explanations for this. First, a large groove depth requires the incident fields to traverse a larger length of emitters. More absorption takes place than for a shallower groove, leading to decreased excitation of SPP waves near the bottom and therefore less coupling. Second, the third feature may interact with the upper and lower polaritons at greater groove depths in such a way as to reduce the coupling.
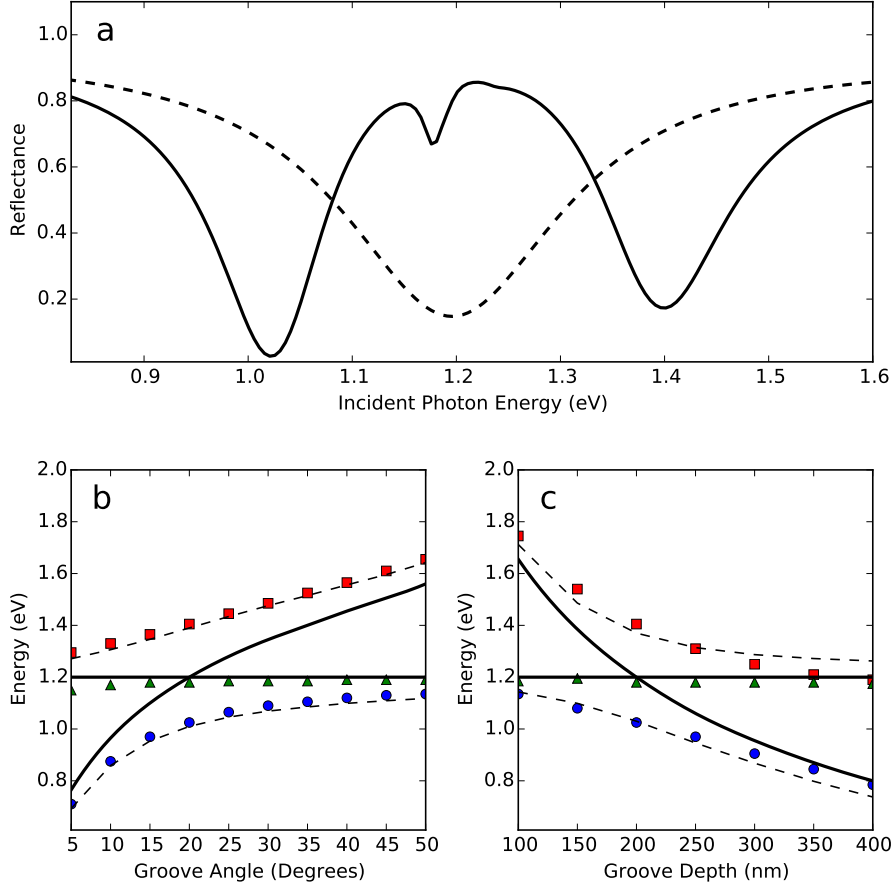
Figure 4.3: Optics of periodic V-grooves coupled to quantum emitters. Panel (a) shows the reflection for bare grooves (dashed line) and the reflection for grooves with emitters is shown as a solid line (with emitters resonant at 1.2 eV). Panel (b) shows the upper polariton (red squares), lower polariton (blue circles), and third resonant mode (green triangles) as a function of the groove angle to sweep the SPP resonance through the emitter resonance. Panel (c) shows the same modes as in panel (b) but as functions of the groove depth to sweep the SPP resonance through the emitter resonance. The horizontal black lines in panels (b) and (c) represent the fixed emitter resonance, the curved black lines represent the SPP energy of the bare grooves for the given geometry, and the dashed lines are values predicted by the coupled oscillator model. The density of emitters is 3×10^{26} emitters/m^3.

While it is clear that many of the emitters are coupled to the SPPs, some may remain coupled only to the incident field (Agranovich and La Rocca, 2005) and thus act as an absorbing layer. To better understand the overall optical coupling in spatially distributed inhomogeneous hybrid systems, two different arrangements of emitters

are simulated: "full" grooves and "hollowed" grooves, as shown in Fig. 4.4a. In the "full" grooves, the region of the grooves occupied by emitters is completely full of emitters up to a given height, whereas in "hollowed" grooves, the region of emitters extends out sideways from either side of the groove by a fixed width (referred to as "width of emitters" from here on). The grooves are illuminated with CW fields at 1.2 eV (uniform intensity, Fig. 4.2b) or 2.255 eV (localized intensity, Fig. 4.2c).

The Rabi splitting is observed as the area occupied by the emitters is varied. Fig. 4.4b shows that, for the distributed resonance, there is relatively little difference in Rabi splitting when the same amount of area is occupied by the emitters for either full or hollowed grooves, which demonstrates that the entire volume of emitters is indeed coupled to the SPP waves. Given that coupling strength depends on field strength, this is reasonable in light of the uniform distribution of intensity in the bare groove at this frequency; the same Rabi splitting is achieved regardless of where a given area of emitters is placed in the groove. In other words, for the distributed resonance we expect (and observe) the Rabi splitting to scale with the number of emitters, which is represented by the area within the groove that is occupied by the emitters. Fig. 4.4c shows that, for the localized resonance, a large increase in Rabi splitting occurs as the area is increased from the bottom, but then it levels off to a constant value well before the emitters reach the top of the groove. This is exactly what is expected as the strong fields near the bottom of the groove give the strongest coupling. The constant value of Rabi splitting is smaller for the lowest width of emitters (10 nm) and this occurs because the fields above the bottom of the groove are weaker but not zero (hence a larger hollow region loses some of the emitters coupled to those weaker fields). A small jump occurs at the end of each graph in Fig. 4.4c and this is due to the increased fields at the sharp corners of the groove. This jump occurs at smaller areas for more hollowed grooves as they occupy less area when they extend to the top
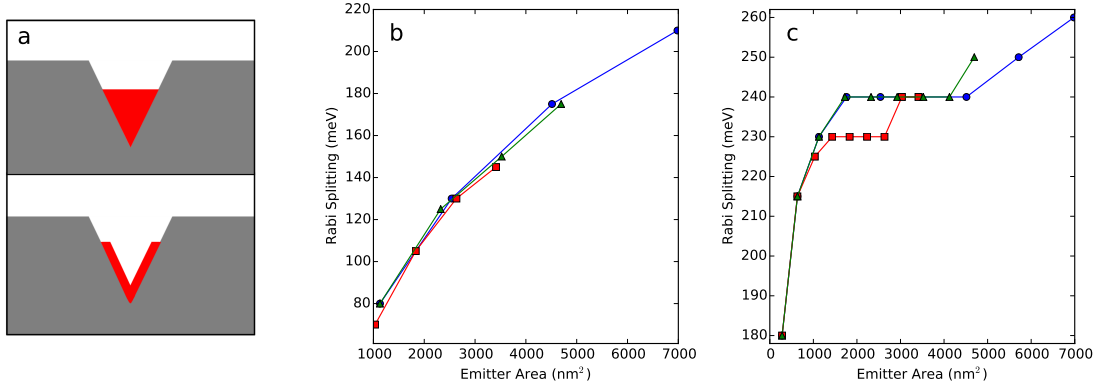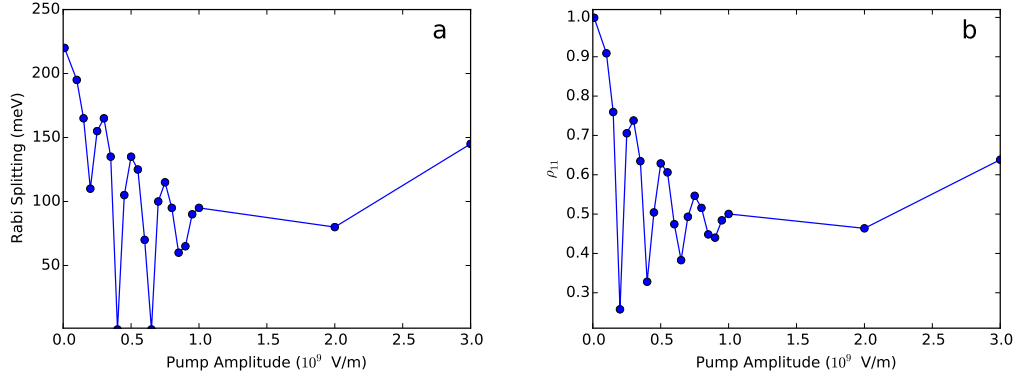
Figure 4.4: Spatially dependent coupling. The density of emitters is 10^{26} emitters/m^3, the transition energy is 1.2 eV, and the pure dephasing time is 400 fs. As the height of the molecular aggregate is increased, the coupling for the distributed resonance increases continuously whereas that for the localized resonance levels off quickly. Panel (a) shows schematics of "full" grooves versus "hollowed" grooves. Panel (b) shows the Rabi splitting as a function of the area occupied by the emitters for the more spatially distributed 1.2 eV resonance, where blue circles indicate full grooves, red squares indicate hollowed grooves (width of emitter region is 10nm) and green triangles indicate hollowed grooves (width of emitter region is 15 nm). Panel (c) is the same as panel (b) except the data is shown for the more localized 2.255 eV resonance. The pure dephasing time is 600 fs.

of the groove.

All simulations discussed above begin with all of the emitters in the ground state. One can pump the system by sending in a high-intensity pulse, thereby inducing Rabi oscillations in the emitters. Below the time dynamics of a pumped hybrid system is discussed. In particular, we observe how Rabi splitting depends on the ground state population at the end of the pump.

First, the system is pumped with a 30 fs pulse, and it is subsequently probed with a short, low-intensity pulse as it was in the linear regime. The Rabi splitting is obtained from the reflection spectrum by calculating the difference in resonant energies for the upper and lower polaritons. Fig. 4.5a shows Rabi splitting as a function of pump amplitude at the end of the pump. Fig. 4.5b shows the ground state population, averaged over the entire region of emitters at the end of the pump, as a function

Figure 4.5: Pump-probe dynamics. Panel (a) shows Rabi splitting as a function of pump amplitude. Each value is obtained by launching a short, low-intensity probe pulse immediately after the pump. Panel (b) shows ground state population, ρ_{11}, as a function of pump amplitude. This value is averaged over the entire region occupied by emitters and obtained at the end of the pump. The density of emitters is 10^{26} emitters/m^3, the pure dephasing time is 400 fs, the transition energy is 1.2 eV, and the duration of the pump is 30 fs.

of pump amplitude. Notice how the plot in Fig. 4.5b oscillates; this is because the area under the pump pulse (which depends on both pump amplitude and duration) determines the number of Rabi cycles (Allen and Eberly, 1975). Thus different pump amplitudes generate greater or fewer Rabi oscillations, leading to different values of the ground state population at the end of the pump.

Fig. 4.5 indicates that the amount of Rabi splitting depends on the ground state population of the emitters, ρ_{11}. We see that a large excited population of emitters in the entire groove will reduce or eliminate the Rabi splitting whereas a smaller excited population will yield larger Rabi splitting. We speculate that the coupling may take on a different character in the non-linear regime, perhaps to the extent that Rabi splitting is not the only indicator of coupling strength. Further investigation of the optical properties of excited emitters coupled to plasmons is clearly warranted. Also, the reduction of Rabi splitting with increasing excited state population may be related to saturation effects that are observed (Vasa *et al.*, 2010), in which an

increasing pump energy "reduces the exciton transition dipole density", resulting in the upper and lower polaritons acquiring structure and (for the larger pump energies) causing uncoupling of SPPs and emitters from one another.

Although the changes of ρ_{11} are in step with changes in Rabi splitting, large decreases of ρ_{11} do not always give a correspondingly large decrease in Rabi splitting and this can be understood in terms of the non-uniformity of ρ_{11} throughout the groove. In particular, the pumping fields arrive at deeper parts of the groove later than they arrive at the top and the Rabi oscillations are not perfectly in phase with one another along the length of the groove due to retardation. Additionally, the SPP fields are inhomogeneous throughout the groove. Thus, the spatially averaged value of ρ_{11} after the pump gives a good, though not ideal, indication of the subsequent coupling to SPP fields.

Fig. 4.6a shows a spatial distribution of ρ_{11} at the end of 70 fs long pump. A clear strong spatial variation of the ground state population is seen. In fact, the variations of the ground state population are oscillations whose wavelength varies somewhat over the region of emitters. One might surmise that the wavelength of these oscillations is on the order of that of the pump, but it is actually significantly smaller. To investigate this further, we numerically solve the Schrödinger equation for a one-dimensional region of two-level atoms (finite along, say, the z-axis while infinite along two others) subject to excitation from a pump.

Because we consider a one-dimensional region, retardation effects must be included by using the retarded time $t - z/v$, where v is the speed of light in the medium in the expression for the pulse. The retardation effects are revealed to be the cause of the spatial modulations of the ground state population, as shown in Fig. 4.6b: the temporal oscillations of the ground state probability are similar between adjacent spatial points, but slightly shifted. Hence at a given time, adjacent points have
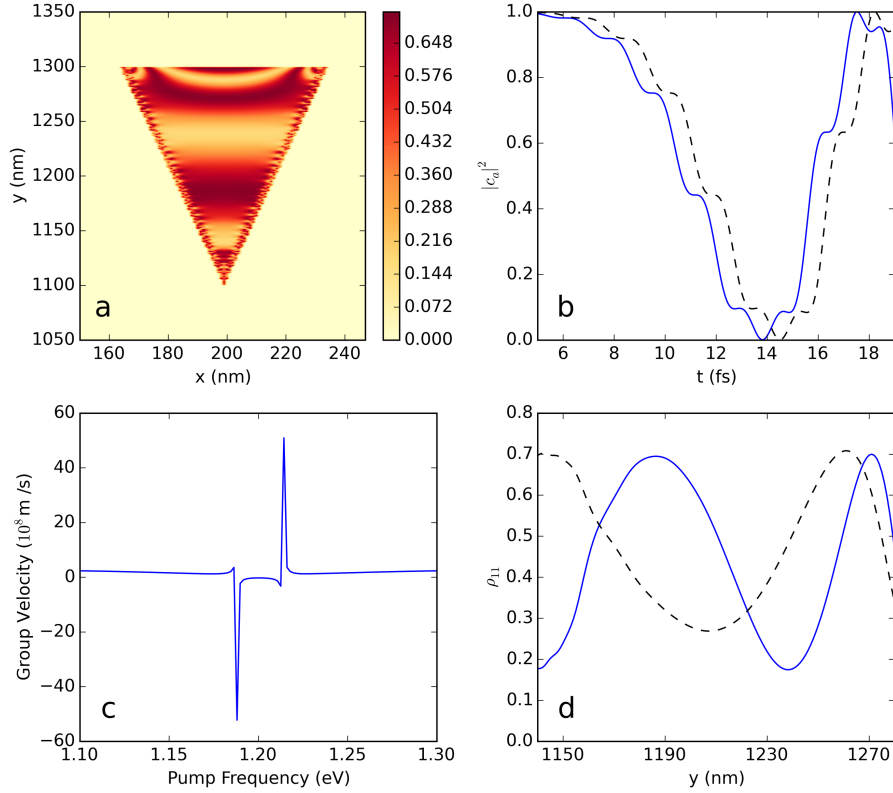
Figure 4.6: Spatial modulations of the molecular ground state. Each run consists of a 70 fs pump applied to the hybrid V-grooves system. The simulations shown in panels (a), (c), and (d) are run with FDTD and the Liouville-von Neumann equation whereas that in panel (b) is run by numerically integrating the Schrodinger equation for a two-level atom. For panels (a), (c), and (d) the density is 10^{26} emitters/m^3, the pump amplitude is 7×10^8 V/m, and the dephasing time is 400 fs. Panel (a) shows the fraction of emitters in the ground state. The characteristic length of spatial modulations is much less than the pump wavelength of 1033 nm. Panel (b) shows oscillations of the ground state population for two emitters separated by 50 nm. Panel (c) shows that the group velocity at the transition frequency is less than c. The plot displays two spikes. We hypothesize that these are numerical artifacts associated with taking a finite derivative of the index of refraction in the region of anomalous dispersion, as runs performed with a smaller spatial step result in smaller spikes. Panel (d) shows the ground state population as a function of coordinate for the system pumped on resonance (1.2 eV, solid line) and slightly off resonance (1.15 eV, dashed line).

slightly different values of ground state probability. To further elucidate this idea, we generated larger phase shifts in the temporal oscillations between nearby points by adjusting two parameters: the pump amplitude and the propagation velocity of light

in the emitter region.

For a larger pump amplitude, each emitter will undergo Rabi flopping more rapidly in time. Thus a given phase shift between adjacent locations will lead to a larger shift in the ground state population between those two locations. This was observed in our simulations: in general, increasing the pump amplitude leads to an increase in the number of spatial oscillations of the ground state population over the region of emitters. For a slower group velocity, the pump takes longer to reach an adjacent point, causing the temporal oscillations between two adjacent points to acquire a larger phase difference. Our simulations allow for the adjustment of the group velocity of light in the emitter region, and we see that a decrease in the group velocity results in a greater number of spatial oscillations relative to a larger speed of light.

Fig. 4.6c shows that group velocity is decreased (in fact, negative since most emitters are inverted) at the transition frequency of 1.2 eV, and it is higher away from resonance. A negative group velocity is possible in inverted systems and has been experimentally observed (Wang *et al.*, 2000). It is stated that this occurs when different frequency components of a pulse interfere with one another (in a region of anomalous dispersion) in such a way as to cause a resonant pulse to be advanced relative to a non-resonant pulse traveling at *c*. We are assured by Siddiqui and Mojahedi (2003) that this does not violate causality and that it occurs because the early parts of the pulse are reshaped to resemble the later pulse. Furthermore, Woodley and Mojahedi (2003) point out that in passing through a medium with negative group velocity, the information transmitted by the pulse front *suffers a positive and causal delay*. Our system was pumped (in separate runs) both on and off of resonance and Fig. 4.6d shows that the wavelength of the spatial oscillations for the *off resonance* pump is indeed increased relative to the *on resonance* pump on account of the latter having a slower group velocity.

All of these results indicate that retardation effects give rise to spatial oscillations in the ground state population of the emitters contained within the groove. The larger fields of the surface plasmons and the slower group velocity within the emitter region surely enhance these spatial oscillations. It may be possible to use this phenomenon to perform a new type of optical design using femtosecond pulses as a tool to craft hybrid systems. Highly inhomogeneous spatial modulations of molecules lead to the modified refractive index, which is appreciably anisotropic. One can envision an exciting opportunity for a new research direction, in which both the geometry of metal nanostructures and pump pulses govern the refractive index of the system. Furthermore one can apply optimization techniques such as genetic algorithms (Brixner and Gerber, 2003), for instance, to design materials with desired optical properties.

4.4   Conclusion

The optical properties of the bare and hybrid V-groove systems have been explored under several different circumstances. Two SPP resonances with entirely different spatial distributions were shown. Optical coupling between quantum emitters and SPP waves was thoroughly characterized by simulating different groove geometries and spatial configurations of emitters' distributions within the grooves. The value of Rabi splitting was shown to vary with the pumping intensity and in accord with the ground state population. An explanation of this awaits a more developed understanding of coupling in the non-linear regime. Spatial oscillations of the ground state population of emitters within the groove are shown to be the result of field retardation. This work puts forth several suggestions for experimental investigation of coupling in hybrid systems, most notably an investigation of the time dynamics of coupling when the system is pumped with different intensities.

Chapter 5

PHOTON ECHOES

5.1   Introduction

The work presented in this chapter will be submitted for publication (Blake and Sukharev, 2016).

Free induction decay is a well-documented phenomenon that was demonstrated in nuclear magnetic resonance (NMR) and is also observed in optics (Allen and Eberly, 1975). A population of two-level emitters can exist in which all emitters have the same "central" transition energy but each is detuned by some amount from this central energy due to inhomogeneous broadening, which can result from conditions such as Doppler shift in individual gas molecules or variations in E-field from point to point in a solid (Mandel and Wolf, 1995).

The total polarization of an ensemble of two-level emitters is of course the sum of each individual contribution from every emitter of the ensemble. Given that the energies of the emitters in the ensemble are described by a distribution, each individual emitter will oscillate at a frequency that is slightly different from the others. As a result, all of the emitters will oscillate in phase at first, but they will all (for a realistic number of emitters) dephase within a characteristic inhomogeneous lifetime and, if left alone, never rephase again (Allen and Eberly, 1975).

However, for times less than the natural lifetime of the emitter, each emitter is still oscillating. If one inverts the system by applying a π pulse, the oscillations will all "run in reverse", resulting in a subsequent rephasing. The ensemble polarizes once again, and a "photon echo" signal is observed.

This technique is widely used in chemistry and is referred to as photon echo spectroscopy. Inhomogeneous effects due to variations in an emitter's surroundings cause each emitter to oscillate at a slightly different frequency than the others, and photon echo spectroscopy "removes" this effect. Any remaining dephasing is irreversible by the echo technique, and is revealed as diminished intensity of the echo (Cho *et al.*, 1992). For example, as the delay in applying the π pulse increases, the natural lifetime of the emitters causes all of their oscillations to decrease, resulting in an echo with lower intensity.

Additionally, the recovery of a signal after dephasing offers prospects for memory storage. In Langer *et al.* (2014), the optical properties are "copied" to a spin system whose lifetime is much longer than that of the optical system thus extending the duration of the system's memory.

We consider an ensemble of two-level emitters and introduce a model that incorporates a distribution of detuned energies. This corresponds to inhomogeneous broadening and will be referred to as such from here on. We discuss the fact that after initial excitation of a point-like ensemble of non-interacting emitters, free induction decay occurs followed by spontaneous rephasing. This spontaneous rephasing is unphysical for a realistic number of emitters and we discuss how to avoid this. We show that application of a $\pi/2$ pulse to a 1-D ensemble followed by application of a π pulse generates a photon echo signal. The density of emitters in this ensemble is varied and the strength of the echo is considered in terms of the transmission and reflection of the ensemble. Finally, we investigate the photon echo of two hybrid systems, metallic slits and a metallic cylinder, each combined with inhomogeneously broadened two-level emitters. The schematics of each system are shown in Fig. 5.1.
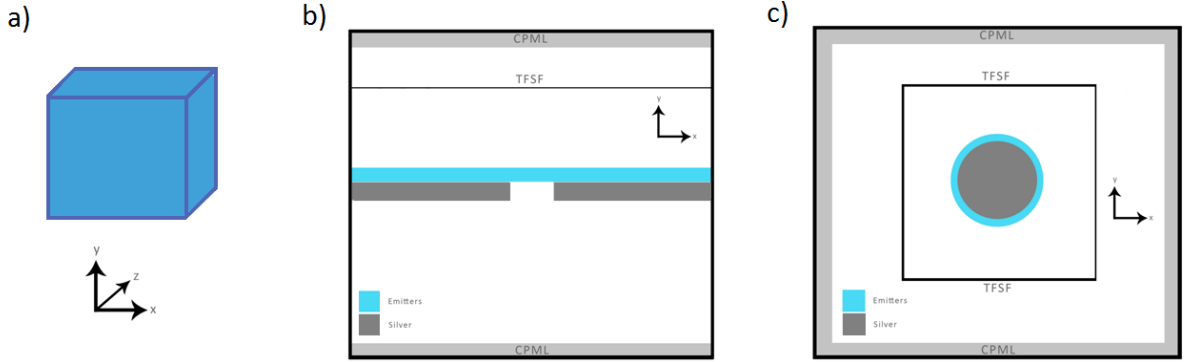
Figure 5.1: Schematics of the systems under consideration. a) 1-D ensemble. b) Slits with emitters. c) Core-shell nanoparticle.

5.2 Model

As in all previous sections, the FDTD method is used to generate and propagate fields and the Liouville-von Neumann equation describes the time dynamics of the emitters.

A normalized Gaussian distribution G is used to describe the energies of the atoms in the ensemble. The width of this distribution is referred to as the inhomogeneous broadening. The distribution is normalized such that:

$$\sum_{kk} G(kk) = 1 \tag{5.1}$$

where kk corresponds to a specific energy in the distribution. This distribution is multiplied by a given density, giving the density of atoms at each energy.

The following set of parameters describing a quantum emitter is used in this paper: the transition dipole moment is 10 Debye and the radiationless lifetime of the excited state is 1 ps.

5.3   Results and Discussion

In the absence of damping processes, the polarization of an ensemble of emitters with a distribution of only a few energies (compared to a realistic number) excited by a $\pi/2$ pulse corresponding to the central energy will undergo free induction decay and then spontaneously rephase periodically afterward. As the number of energies (points) on the Gaussian curve is increased, the time between rephasings increases. For a realistic number of emitters, the rephasing time of course becomes infinite (Allen and Eberly, 1975). We therefore work within an amount of time for which no spontaneous rephasings occur.

The $\pi/2$-π-echo sequence is shown in Fig. 5.2. τ_1 corresponds to the time between the maximum of the $\pi/2$ pulse and the π pulse, and τ_2 corresponds to the time between the maximum of the π pulse and the maximum of the echo. These times are roughly equal as they should be (Mandel and Wolf, 1995). An ensemble is excited by a $\pi/2$ pulse which then undergoes free induction decay. A π pulse is applied, and the maximum of the photon echo signal is observed at time $\tau_1 + \tau_2$ after the maximum of the $\pi/2$ pulse. In this simulation, emitters at a point are driven by external fields but do not emit their own fields and thus, the polarization current dP/dt is plotted and used as an indication of rephasing.

The ensemble treated thus far has been a collection of emitters at a single point. In order to determine the influence of collective effects on the echo amplitude, an extended one-dimensional ensemble of emitters is driven by incident fields. We allow emitters within the ensemble to interact with each other through the fields that each one emits via polarization current.

In the linear regime, the transmission and reflection broaden and flatten as the inhomogeneous broadening is increased. A representative transmission spectrum is

60
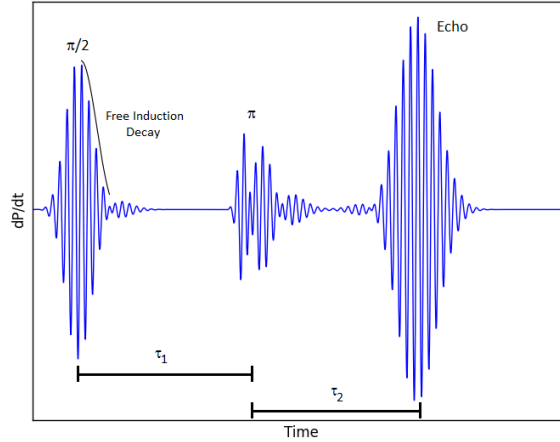
Figure 5.2: The $\pi/2$-π-echo sequence. The photon echo signal occurs after application of a $\pi/2$ pulse followed by a π pulse to an ensemble of two-level emitters all located at a single point with a Gaussian distribution of energies.

shown in Fig. 5.3. More importantly, the transmission decreases toward 0 and the reflection increases toward 1 as the density increases beyond 10^{26} m^{-3} as demonstrated in Puthumpally-Joseph *et al.* (2014). Distortion is observed in the edges of the spectral features due to increasing interference between the reflected signals from varying depths of the ensemble. This is also noted in Puthumpally-Joseph *et al.* (2014).

We apply the $\pi/2$ and π pulses, then record the integral of the echo field squared on both the input and output sides. This is performed for several densities, ensemble lengths, and values of inhomogeneous broadening and the results are shown in Fig. 5.4. On both sides of the ensemble, the echo amplitude increases with density for lower densities but, in many instances, decreases sharply at higher densities. This can be understood in terms of how the transmission and reflection of the ensemble vary with density. At higher densities, the reflection approaches 1 and the transmission becomes very small as previously discussed. Thus, the driving fields don't make it as far into the ensemble for higher densities.

This is verified in Fig. 5.5 where it is seen that, for a higher density, the ground

61
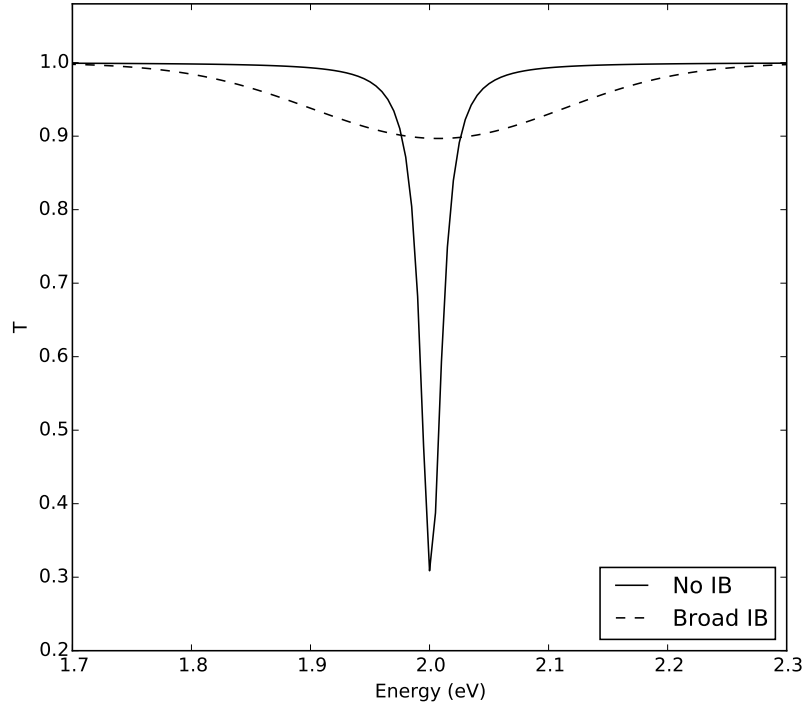
Figure 5.3: Transmission spectrum for a 1-D ensemble of interacting emitters with and without inhomogeneous broadening (IB). Length is 200 nm and density is 10^{25} m^{-3}.

state population ρ_{11} tends toward 1 as we look farther into the ensemble; the driving fields are smaller and therefore do not drive the emitters through $\pi/2$ oscillations. With this in mind, it makes sense that the echo on the output side drops off at higher densities: more and more of the ensemble (toward the output side) ceases to participate in the echo at higher densities, and the echo from the input side is not able to travel through the ensemble to the output side. Furthermore, we see that for the shortest (200 nm) ensembles, the echo signal continues to increase or does not drop as sharply on the input side, as there is less interference from deeper regions of the ensemble.

We now turn our attention to a hybrid system of metallic slits and two-level

62
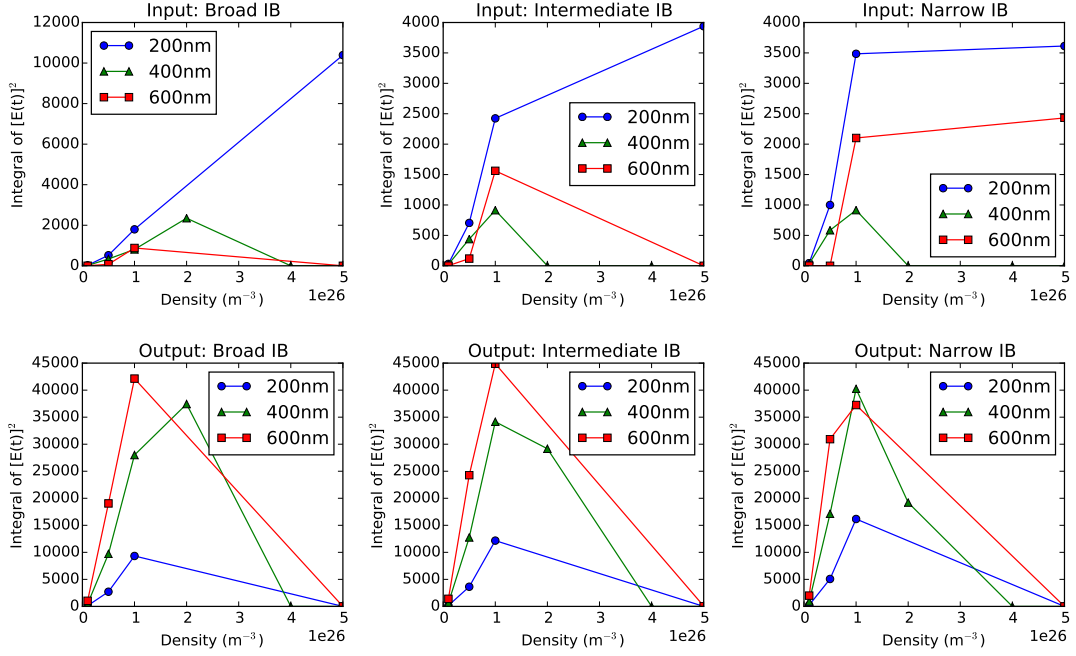
Figure 5.4: Photon echo energy on the input and output sides of a 1-D ensemble. Density, ensemble length, and inhomogeneous broadening are varied. The signal increases with density at lower densities and in several cases drops sharply at higher densities, which is attributed to highly increased reflection.
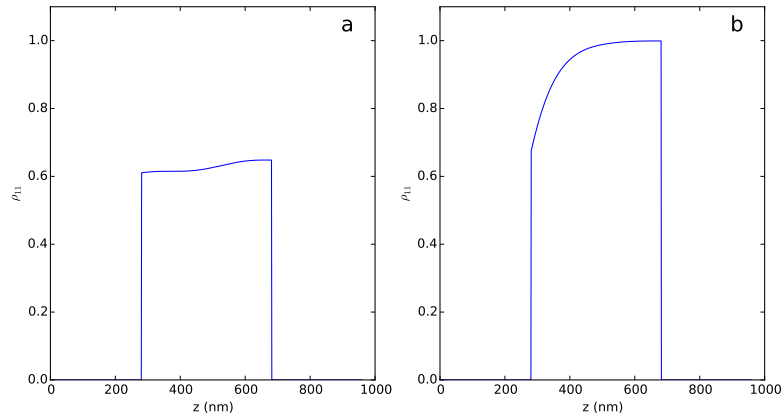
Figure 5.5: Ground state population along the 1-D ensemble of emitters. The ensemble is 400 nm in length. Density is: a) 10^{25} m^{-3} b) 10^{26} m^{-3}
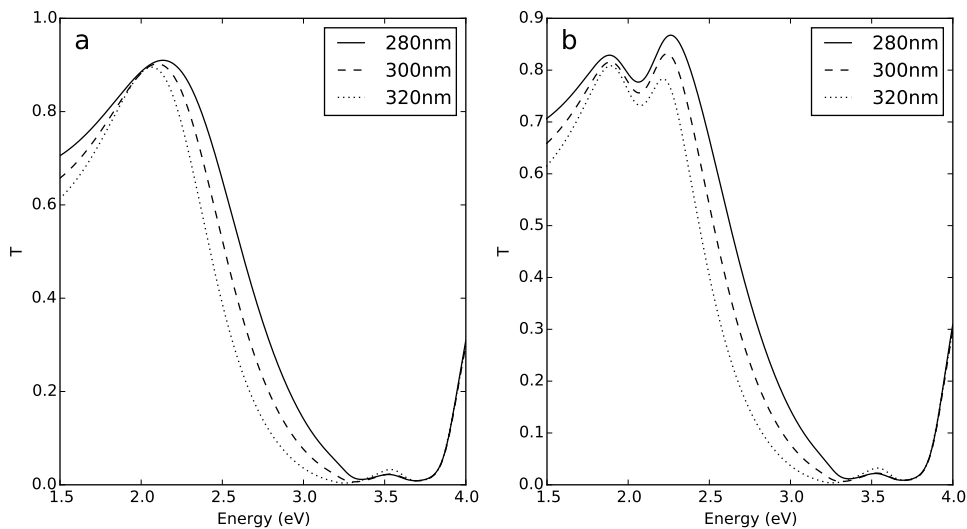
Figure 5.6: Linear transmission spectra of slits system. Film thickness is 200 nm and slit width is 140 nm. a) Bare metal slits with different periods showing SPP resonance. b) Hybrid slits, whose emitters include inhomogeneous broadening, with different periods.
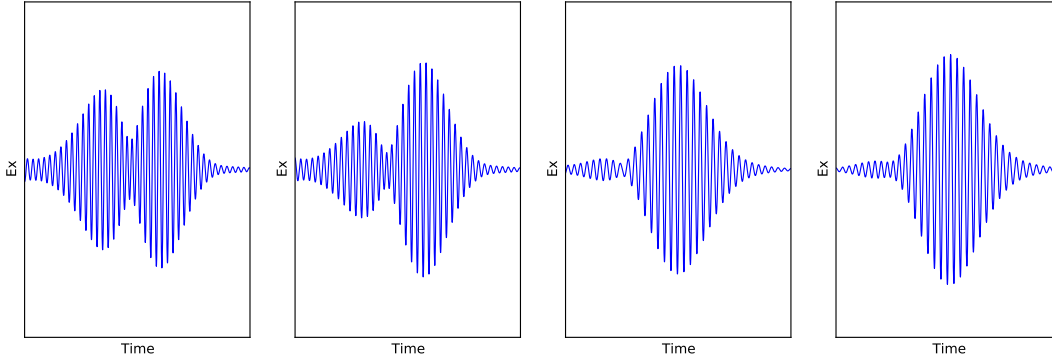
emitters with inhomogeneous broadening. The bare metallic grating exhibits a surface plasmon resonance in the form of enhanced transmission and decreased reflection. Adding two-level emitters with no inhomogeneous broadening and probing in the linear regime results in Rabi splitting into an upper and lower polariton. When the two-level emitters are given inhomogeneous broadening and we again probe in the linear regime, the Rabi splitting is still present but it is smoother and more gentle than without the distribution. Fig. 5.6 shows transmission spectra for bare slits and for hybrid slits whose emitters are inhomogeneously broadened.

We apply the $\pi/2$ - π - echo sequence to the hybrid system and observe the x-component of the electric field on both the input and output side of the system for the duration of the echo. What is seen is very different from the echo generated by the 1-D ensemble: for this system, an echo with a double-peaked structure is observed (Figs. 5.7 and 5.9), and an FFT of the echo signal reveals two peaks. We proceed to

Figure 5.7: Double-peaked photon echo from hybrid system consisting of metallic slits and two-level emitters with inhomogeneous broadening. The density is 10^{26} m^{-3} and the thickness of the film of emitters is 20 nm. A spacer of varying thickness is inserted between the film and the slits, and the double-peaked structure gradually reduces to a single peak as the spacer thickness is increased. The spacer lengths (from left to right) are 0 nm, 5 nm, 25 nm, and 75 nm.

show that this double-peaked structure has its origin in the interaction between the surface plasmons and the emitters.

Surface plasmons are intense and localized to within nanometers of the metallic structure. In order to ascertain whether the double-peak is influenced by surface plasmons, we insert a (vacuum) spacer layer of variable thickness between the film of emitters and the slits. As the spacer thickness is increased, the film is moved into progressively weaker plasmon fields. As shown in Fig. 5.7, the double-peaked structure of the echo gradually disappears as the spacer thickness is increased.

Proceeding with the idea that the double peak is caused by surface plasmons, we consider a different hybrid system consisting of a metallic cylinder surrounded by a shell of two-level emitters with inhomogeneous broadening. The bare metallic cylinder shows a plasmon resonance at 3.59 eV; the scattered field intensity is enhanced at this energy. Linear spectra of scattered field intensity are shown in Fig. 5.8 for a bare metal cylinder and for a hybrid cylinder with inhomogeneously broadened emitters.
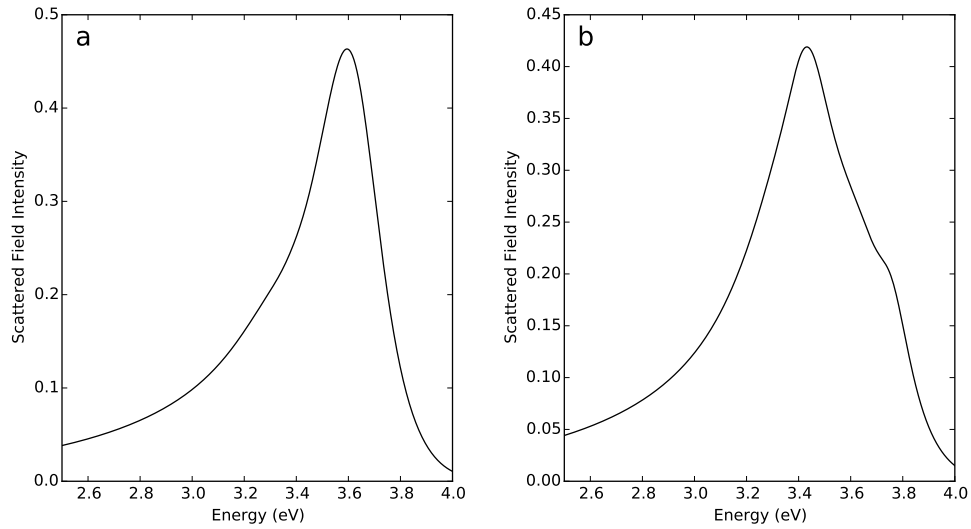
Figure 5.8: Linear spectra of core-shell system. Cylinder radius is 25 nm. a) Bare metal cylinder showing SPP resonance. b) Hybrid system, whose emitters include inhomogeneous broadening.
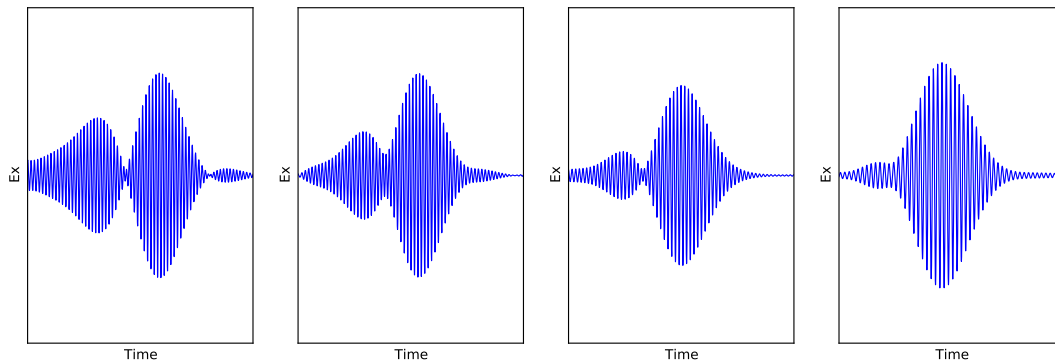
Figure 5.9: Photon echo from a hybrid system consisting of a core-shell cylinder. The core is metallic and the shell consists of two-level emitters with inhomogeneous broadening. In order to illustrate the plasmonic origin of the double-peaked echo structure, the central energy of the two-level emitter distribution is detuned from the plasmon resonance of 3.59 eV. The central energies are (from left to right) 3.50 eV, 3.40 eV, 3.30 eV, and 3.09 eV.

66
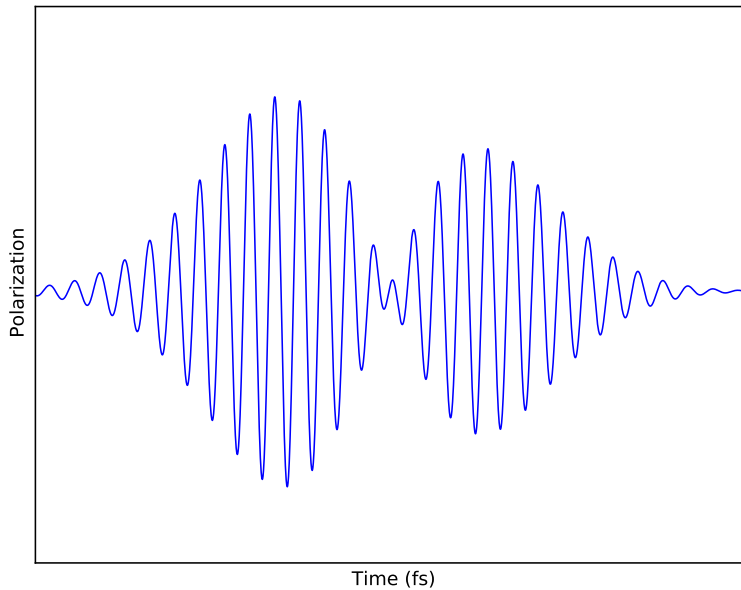
Figure 5.10: Double-peaked echo from an ensemble of inhomogeneously broadened emitters located at a point. The double-peaked photon echo is reproduced by driving the emitters with a superposition of pulses with two different driving frequencies.

To minimize the interaction between the two-level emitters and the surface plasmons, the central energy of the distribution of emitters is detuned by varying amounts from the plasmon resonance. As shown in Fig. 5.9, this results in the gradual loss of the double-peak structure in the echo. Detuning was also applied to the hybrid slits system, both by adjusting the emitters' central energy as well as adjusting the slit period (and therefore altering the surface plasmon energy). As expected, the double-peak structure disappeared in each instance as detuning was increased.

We are confident that the double-peaked echo is caused by surface plasmons, and we further speculate that the double peak structure is the signature of the upper and lower polaritons that form as a result of strong coupling between surface plasmons and emitters. A precise correspondence between the upper and lower polariton energies and the two peaks in the echo spectrum was difficult to obtain for several reasons.

First, the energies of the peaks in the FFT of the echo signal were very sensitive to the sampling range. As the range was changed, the double-peak structure remained roughly the same but the energies of the peaks shifted. Secondly, we sought a relation between the upper and lower polariton amplitudes in the linear spectrum versus the height of the FFT peaks, but a larger peak in the linear spectrum does not necessarily correspond to a stronger peak in the FFT spectrum as the echo depends on rephasing, and the upper and lower polariton energies may be asymmetrically detuned from the central energy, leading to a weaker rephasing of one component or the other. Finally, spatial inhomogeneities of the fields also complicate the matter in that some emitters may be driven through more or less than the "correct" $\pi/2$ - π sequence. In spite of these difficulties, we find some reassurance in that a double-peaked echo is able to be reproduced by driving emitters at a point with a superposition of pulses with slightly different driving energies as shown in Fig. 5.10. Though simpler, this is analogous to a hybrid system being driven by its hybrid modes.

5.4   Conclusion

We have demonstrated that our numerical methods reproduce photon echoes and we have characterized the echo from a one-dimensional ensemble in terms of density, ensemble length, and amount of inhomogeneous braodening. The double-peaked echo from two hybrid systems is shown by various different means to be of plasmonic origin, with the double-peaked structure likely resulting from the hybrid modes of the system.

Chapter 6

CONCLUSION AND FUTURE WORK

In this work, a method of launching obliquely incident waves was implemented for hybrid systems. It is limited in some situations, but still proves insightful in studying the coupling between emitters and a metallic nanoscale structure. V-grooves were thoroughly studied: the coupling in the linear regime was characterized by varying the groove parameters and also by placing emitters within the groove in different geometries and observing the coupling at the resonance energies. In this system, coupling strength is in step with ground state population. Slow light is responsible for spatial variations of the ground state population within the emitters, as verified by adjusting parameters that determine field retardation. Photon echoes from an ensemble of inhomogeneously broadened emitters at a point were successfully simulated, followed by the analysis of the photon echo from a 1-D ensemble of interacting emitters. Finally, the photon echoes from two hybrid systems were observed to have a unique double-peaked structure, due in all probability to the coupling between surface plasmons and the emitters.

It would be intriguing to carry out experiments with v-grooves in both the linear and non-linear regimes to see how well the results correspond to those of the simulations. Assuming that an array of v-grooves could be fabricated as in the simulations (such that the array supports a mode with uniform intensity and one with localized intensity), the Rabi splitting corresponding to emitters carefully distributed in various spatial arrangements within each groove should show no dependence upon the arrangement for the uniform mode whereas it should for the localized mode. A pump-probe setup showing Rabi splitting as the pump amplitude is varied would re-

veal changes in coupling due to the emitters being driven through Rabi oscillations. A series of simulations that takes advantage of slow light could be run in which the spatial oscillations of the ground state population are specifically arranged in various ways by a short, high-intensity pump, "crafting" different configurations of the emitters within the groove and identifying their corresponding optical properties. It would be exciting to compare these predicted properties with experimental work.

Photon echoes in hybrid systems and 1-D ensembles of interacting emitters are relatively unexplored. An experimental exploration of the photon echo in 1-D ensembles of interacting emitters is called for, as a very simple prediction is made: as molecular density increases, the echo strength on the output side will increase until reflection increases substantially, at which point the echo strength plummets. The photon echo associated with a hybrid system especially warrants further theoretical and experimental attention: simply observing the double-peaked structure of the photon echo in a hybrid system would be significant, and ascertaining the influence of plasmons on the echo structure (by adding a spacer layer or by detuning the plasmon and emitter resonances) would be even more so. Simulating different types of systems or adjusting the $\pi/2$ - π sequence in the simulations as well as the molecular parameters could provide a more accurate correspondence between the upper and lower polaritons and the energy of each peak in an FFT of the echo.

All in all, many of the theoretical results described in this work present compelling opportunities for experimental work and for further theoretical study.

REFERENCES

Agranovich, V. and G. La Rocca, "Electronic excitations in organic microcavities with strong lightäìmatter coupling", Solid State Commun **135**, 9Äì10, 544–553 (2005).

Agranovich, V. M., M. Litinskaia and D. G. Lidzey, "Cavity polaritons in microcavities containing disordered organic semiconductors", Phys. Rev. B **67**, 085311, URL `http://link.aps.org/doi/10.1103/PhysRevB.67.085311` (2003).

Allen, L. and J. H. Eberly, *Optical Resonance and Two-Level Atoms* (John Wiley & Sons, Inc., 1975).

Aminian, A. and Y. Rahmat-Samii, "Spectral fdtd: A novel techique for the analysis of oblique incident plane wave on periodic structures", IEEE Trans. Antennas Propag (2006).

Antosiewicz, T. J., S. P. Apell and T. Shegai, "Plasmon-exciton interactions in a core-shell geometry: From enhanced absorption to strong coupling", ACS Photonics **1**, 5, 454–463, URL `http://pubs.acs.org/doi/abs/10.1021/ph500032d` (2014).

Avrutsky, I., Y. Zhao and V. Kochergin, "Surface-plasmon-assisted resonant tunneling of light through a periodically corrugated thin metal film", Opt. Lett. **25**, 9, 595–597, URL `http://ol.osa.org/abstract.cfm?URI=ol-25-9-595` (2000).

Barnes, W. L., A. Dereux and T. W. Ebbesen, "Surface plasmon subwavelength optics", Nature **424**, 6950, 824–830, URL `http://dx.doi.org/10.1038/nature01937` (2003).

Bellessa, J., C. Bonnand, J. Plenet and J. Mugnier, "Strong coupling between surface plasmons and excitons in an organic semiconductor", Phys. Rev. Lett. **93**, 036404, URL `http://link.aps.org/doi/10.1103/PhysRevLett.93.036404` (2004).

Berrier, A., R. Cools, C. Arnold, P. Offermans, M. Crego-Calama, S. H. Brongersma and J. Gmez-Rivas, "Active control of the strong coupling regime between porphyrin excitons and surface plasmon polaritons", ACS Nano **5**, 8, 6226–6232, URL `http://dx.doi.org/10.1021/nn201077r` (2011).

Bhushan, B., ed., *Encyclopedia of Nanotechnology* (Springer, 2012).

Blake, A. and M. Sukharev, *From Atomic to Mesoscale: The Role of Quantum Coherence in Systems of Various Complexities*, chap. Linear Optical Properties of Periodic Hybrid Materials and Oblique Incidence: A Numerical Approach, pp. 149–164 (World Scientific, 2015a).

Blake, A. and M. Sukharev, *Nanoscale Materials and Devices for Electronics, Photonics, and Solar Energy*, chap. Optics of Hybrid Nanomaterials in the Strong Coupling Regime, pp. 263–274 (Springer, 2015b).

Blake, A. and M. Sukharev, "Surface plasmon polaritons in periodic arrays of v-shaped grooves strongly coupled to quantum emitters", Phys. Rev. B **92**, 035433, URL `http://link.aps.org/doi/10.1103/PhysRevB.92.035433` (2015c).

Blake, A. and M. Sukharev, "Photon echo in exciton-plasmon nanomaterials: A signature of strong coupling", Submitted to J. Chem. Phys. (2016).

Brixner, T. and G. Gerber, "Quantum control of gas-phase and liquid-phase femtochemistry", ChemPhysChem **4**, 5, 418–438, URL `http://dx.doi.org/10.1002/cphc.200200581` (2003).

Cho, M., N. F. Scherer, G. R. Fleming and S. Mukamel, "Photon echoes and related four wave mixing spectroscopies using phase locked pulses", The Journal of Chemical Physics **96**, 8, 5618–5629, URL `http://scitation.aip.org/content/aip/journal/jcp/96/8/10.1063/1.462686` (1992).

Curto, A. G., G. Volpe, T. H. Taminiau, M. P. Kreuzer, R. Quidant and N. F. van Hulst, "Unidirectional emission of a quantum dot coupled to a nanoantenna", Science **329**, 5994, 930–933 (2010).

Ebbesen, T. W., H. J. Lezec, H. F. Ghaemi, T. Thio and P. A. Wolff, "Extraordinary optical transmission through sub-wavelength hole arrays", Nature **391**, 6668, 667–669, URL `http://dx.doi.org/10.1038/35570` (1998).

Efros, A. L. and A. L. Efros, "Interband absorption of light in a semiconductor sphere", Sov. Phys. Semicond. **16**, 772 (1982).

Ekimov, A. I. and A. A. Onushchenko, "Quantum size effect in three-dimensional microscopic semiconductor crystals", JETP Letters **34**, 345 (1981).

Fernandez-Cuesta, I., R. B. Nielsen, A. Boltasseva, X. Borrise, F. Perez-Murano and A. Kristensen, "Excitation of fluorescent nanoparticles by channel plasmon polaritons propagating in v-grooves", Appl Phys Lett **95**, 20, URL `http://scitation.aip.org/content/aip/journal/apl/95/20/10.1063/1.3262945` (2009).

Garcia de Abajo, F., "*Colloquium* : Light scattering by particle and hole arrays", Rev. Mod. Phys. **79**, 1267–1290, URL `http://link.aps.org/doi/10.1103/RevModPhys.79.1267` (2007).

Gray, S. K. and T. Kupka, "Propagation of light in metallic nanowire arrays: Finite-difference time-domain studies of silver cylinders", Phys. Rev. B **68**, 045415, URL `http://link.aps.org/doi/10.1103/PhysRevB.68.045415` (2003).

Griffiths, D. J., *Introduction to Electrodynamics* (Prentice Hall, 1998).

Haes, A. J., W. P. Hall, L. Chang, W. L. Klein and R. P. Van Duyne, "A localized surface plasmon resonance biosensor: first steps toward an assay for alzheimer's disease", Nano Lett. **4**, 6, 1029–1034, URL `http://dx.doi.org/10.1021/nl049670j` (2004).

Harms, P. and R. Mittra, "Implementation of the periodic boundary condition in the finite-difference time-domain algorith for fss structures", IEEE Trans. Antennas Propag (1994).

Haroche, S., "Nobel lecture: Controlling photons in a box and exploring the quantum to classical boundary", Rev. Mod. Phys. **85**, 1083–1102, URL `http://link.aps.org/doi/10.1103/RevModPhys.85.1083` (2013).

Hessel, A. and A. A. Oliner, "A new theory of wood's anomalies on optical gratings", Appl. Optics (1965).

Hoa, X., A. Kirk and M. Tabrizian, "Towards integrated and sensitive surface plasmon resonance biosensors: A review of recent progress", Biosensors and Bioelectronics **23**, 2, 151–160, URL `http://www.sciencedirect.com/science/article/pii/S0956566307002710` (2007).

Homola, J., S. S. Yee and G. Gauglitz, "Surface plasmon resonance sensors: review", Sensors and Actuators B: Chemical **54**, 12, 3–15, URL `http://www.sciencedirect.com/science/article/pii/S0925400598003219` (1999).

Hutchison, J. A., D. M. O'Carroll, T. Schwartz, C. Genet and T. W. Ebbesen, "Absorption-induced transparency", Angew Chem Int Edit **50**, 9, 2085–2089, URL `http://dx.doi.org/10.1002/anie.201006019` (2011).

Jain, P. K., X. Huang, I. H. El-Sayed and M. A. El-Sayed, "Review of some interesting surface plasmon resonance-enhanced properties of noble metal nanoparticles and their applications to biosystems", Plasmonics **2**, 3, 107–118, URL `http://dx.doi.org/10.1007/s11468-007-9031-1` (2007).

Jonsson, U., L. Fagerstam, B. Ivarsson, B. Johnsson, R. Karlsson, K. Lundh, S. Lofas, B. Persson, H. Roos and I. Ronnberg, "Real-time biospecific interaction analysis using surface plasmon resonance and a sensor chip technology", BioTechniques **11**, 5, 620627, URL `http://europepmc.org/abstract/MED/1804254` (1991).

Khitrova, G., H. M. Gibbs, M. Kira, S. W. Koch and A. Scherer, "Vacuum rabi splitting in semiconductors", Nat Phys **2**, 2, 81–90, URL `http://dx.doi.org/10.1038/nphys227` (2006).

Langer, L., S. V., Poltavtsev, Y. A., M. Salewski, Y. D. R., G. Karczewski, T. Wojtowicz, A. A. and M. Bayer, "Access to long-term optical memories using photon echoes retrieved from semiconductor spins", Nat Photon **8**, 11, 851–857, URL `http://dx.doi.org/10.1038/nphoton.2014.219` (2014).

Lee, R. T. and G. S. Smith, "A conceptually simple method for incorporating periodic boundary condition into the fdtd method", Microw. Opt. Techn. Let. (2005).

LeRu, E. and P. Etchegoin, *Principles of Surface Enhanced Raman Spectroscopy and Related Plasmon Effects* (Elsevier, 2009).

Lidzey, D. G., D. D. C. Bradley, M. S. Skolnick, T. Virgili, S. Walker and D. M. Whittaker, "Strong exciton-photon coupling in an organic semiconductor microcavity", Nature **395**, 6697, 53–55, URL http://dx.doi.org/10.1038/25692 (1998).

Livneh, N., A. Strauss, I. Schwarz, I. Rosenberg, A. Zimran, S. Yochelis, G. Chen, U. Banin, Y. Paltiel and R. Rapaport, "Highly directional emission and photon beaming from nanocrystal quantum dots embedded in metallic nanoslit arrays", Nano Lett. **11**, 4, 1630–1635, URL http://dx.doi.org/10.1021/nl200052j (2011).

Mandel, L. and E. Wolf, *Optical Coherence and Quantum Optics* (Cambridge University Press, 1995).

Mosor, S., J. Hendrickson, B. Richards, J. Sweet, G. Khitrova, H. Gibbs, T. Yoshie, A. Scherer, O. Shchekin and D. Deppe, "Scanning a photonic crystal slab nanocavity by condensation of xenon", Applied Physics Letters **87**, 141105 (2005).

MSU, URL http://www.pa.msu.edu/~mmoore/Lect34_DensityOperator.pdf (2009).

Mu, W., D. B. Buchholz, M. Sukharev, J. I. Jang, R. P. Chang and J. B. Ketterson, "One-dimensional long-range plasmonic-photonic structures", Opt. Lett. **35**, 4, 550–552, URL http://ol.osa.org/abstract.cfm?URI=ol-35-4-550 (2010).

Pockrand, I., A. Brillante and D. Mobius, "Exciton-surface plasmon coupling: An experimental investigation", The Journal of Chemical Physics **77**, 12, 6289–6295, URL http://scitation.aip.org/content/aip/journal/jcp/77/12/10.1063/1.443834 (1982).

Pusch, A., S. Wuestner, J. M. Hamm, K. L. Tsakmakidis and O. Hess, "Coherent amplification and noise in gain-enhanced nanoplasmonic metamaterials: A maxwell-bloch langevin approach", ACS Nano **6**, 3, 2420–2431, URL http://dx.doi.org/10.1021/nn204692x (2012).

Puthumpally-Joseph, R., M. Sukharev, O. Atabek and E. Charron, "Dipole-induced electromagnetic transparency", Phys. Rev. Lett. **113**, 163603, URL http://link.aps.org/doi/10.1103/PhysRevLett.113.163603 (2014).

Raether, H., *Surface Plasmons on Smooth and Rough Surfaces and on Gratings* (Springer, 1988).

Rich, R. L. and D. G. Myszka, "Advances in surface plasmon resonance biosensor analysis", Current Opinion in Biotechnology **11**, 1, 54–61, URL http://www.sciencedirect.com/science/article/pii/S0958166999000543 (2000).

Salomon, A., C. Genet and T. Ebbesen, "Molecule-light complex: Dynamics of hybrid molecule-surface plasmon states", Angew Chem Int Edit **48**, 46, 8748–8751, URL http://dx.doi.org/10.1002/anie.200903191 (2009).

Salomon, A., R. J. Gordon, Y. Prior, T. Seideman and M. Sukharev, "Strong coupling between molecular excited states and surface plasmon modes of a slit array in a thin metal film", Phys. Rev. Lett. **109**, 073002, URL `http://link.aps.org/doi/10.1103/PhysRevLett.109.073002` (2012).

Schlather, A. E., N. Large, A. S. Urban, P. Nordlander and N. J. Halas, "Near-field mediated plexcitonic coupling and giant rabi splitting in individual metallic dimers", Nano Lett **13**, 7, 3281–3286, URL `http://dx.doi.org/10.1021/nl4014887`, pMID: 23746061 (2013).

Schwartz, T., J. A. Hutchison, C. Genet and T. W. Ebbesen, "Reversible switching of ultrastrong light-molecule coupling", Phys. Rev. Lett. **106**, 196405, URL `http://link.aps.org/doi/10.1103/PhysRevLett.106.196405` (2011).

Siddiqui, O. F. and M. Mojahedi, "Periodically loaded transmission line with effective negative refractive index and negative group velocity", IEEE T Antenn Propag **51**, 10, 2619–2625 (2003).

Søndergaard, T. and S. I. Bozhevolnyi, "Surface-plasmon polariton resonances in triangular-groove metal gratings", Phys. Rev. B **80**, 195407, URL `http://link.aps.org/doi/10.1103/PhysRevB.80.195407` (2009).

Sugawara, Y., T. A. Kelf, J. J. Baumberg, M. E. Abdelsalam and P. N. Bartlett, "Strong coupling between localized plasmons and organic excitons in metal nanovoids", Phys. Rev. Lett. **97**, 266808, URL `http://link.aps.org/doi/10.1103/PhysRevLett.97.266808` (2006).

Sukharev, M., "Computational approach in mathematical optics: Classical, quantum and computational methods", Optics and Photonics News (2012).

Sukharev, M., "Control of optical properties of hybrid materials with chirped femtosecond laser pulses under strong coupling conditions", J. Chem. Phys. **141**, 8, – (2014).

Sukharev, M. and A. Nitzan, "Numerical studies of the interaction of an atomic sample with the electromagnetic field in two dimensions", Phys. Rev. A **84**, 043802, URL `http://link.aps.org/doi/10.1103/PhysRevA.84.043802` (2011).

Sukharev, M., T. Seideman, R. J. Gordon, A. Salomon and Y. Prior, "Ultrafast energy transfer between molecular assemblies and surface plasmons in the strong coupling regime", ACS Nano **8**, 1, 807–817, URL `http://dx.doi.org/10.1021/nn4054528` (2013).

Sukharev, M., P. R. Sievert, T. Seideman and J. B. Ketterson, "Perfect coupling of light to surface plasmons with ultra-narrow linewidths", The Journal of Chemical Physics **131**, 3, –, URL `http://scitation.aip.org/content/aip/journal/jcp/131/3/10.1063/1.3177011` (2009).

Taflove, A. and S. Hagness, *Computational Electrodynamics: The Finite-Difference Time-Domain Method* (Artech House, 2005).

Tang, C. L., *Quantum Electronics* (Academic Press, 1979).

Torma, P. and W. L. Barnes, "Strong coupling between surface plasmon polaritons and emitters: a review", Rep. Prog. Phys. **78**, 1, 013901, URL `http://stacks.iop.org/0034-4885/78/i=1/a=013901` (2015).

Treacy, M. M. J., "Dynamical diffraction in metallic optical gratings", Applied Physics Letters **75**, 5, 606–608, URL `http://scitation.aip.org/content/aip/journal/apl/75/5/10.1063/1.124455` (1999).

Treacy, M. M. J., "Dynamical diffraction explanation of the anomalous transmission of light through metallic gratings", Phys. Rev. B **66**, 195105, URL `http://link.aps.org/doi/10.1103/PhysRevB.66.195105` (2002).

Vasa, P., R. Pomraenke, G. Cirmi, E. De Re, W. Wang, S. Schwieger, D. Leipold, E. Runge, G. Cerullo and C. Lienau, "Ultrafast manipulation of strong coupling in metalàímolecular aggregate hybrid nanostructures", ACS Nano **4**, 12, 7559–7565, URL `http://dx.doi.org/10.1021/nn101973p` (2010).

Vasa, P., W. Wang, R. Pomraenke, M. Lammers, M. Maiuri, C. Manzoni, G. Cerullo and C. Lienau, "Real-time observation of ultrafast rabi oscillations between excitons and plasmons in metal nanostructures with j-aggregates", Nat Photon **7**, 2, 128–132, URL `http://dx.doi.org/10.1038/nphoton.2012.340` (2013).

Wang, L. J., A. Kuzmich and A. Dogariu, "Gain-assisted superluminal light propagation", Nature **406**, 6793, 277–279, URL `http://dx.doi.org/10.1038/35018520` (2000).

Willets, K. A. and R. P. Van Duyne, "Localized surface plasmon resonance spectroscopy and sensing", Annu. Rev. Phys. Chem. **58**, 1, 267–297, URL `http://dx.doi.org/10.1146/annurev.physchem.58.032806.104607` (2007).

Woodley, J. and M. Mojahedi, "Negative group velocity in left-handed materials", in "IEEE Antennas Prop", pp. 643–646 vol. 4 (2003).

Yee, K. S., "Numerical solution of initial boundary value problems involving maxwellís equations in isotropic media", IEEE Trans. Antennas Propag **14**, 3, 302–307 (1966).